

1 **Title:** Top-Down Benchmark of U.S. Methane Inventories Reveals Regional Discrepancies in
2 Activity-Based Estimates

3

4 Authors: John Worden^{1,2,*}, Sudhanshu Pandey^{1,*}, Hannah Nesser¹, Kevin Bowman¹, Colin
5 Harkins^{4,8}, Congmeng Lyu^{4,8}, Joannes D. Maasakkers⁵, Deborah Gordon⁶, Daniel Jacob³, Lucas
6 Estrada³, Daniel J. Varon^{9,3}, James D. East³, Lauren Schmeisser⁶ and Zhen Qu⁷

7 1. Jet Propulsion Laboratory, California Institute of Technology, Pasadena, California,
8 United States

9 2. Joint Institute for Regional Earth System Science and Engineering, University of
10 California, Los Angeles, Los Angeles, California, United States

11 3. Harvard University, Cambridge, Massachusetts, United States

12 4. NOAA Chemical Sciences Laboratory, Boulder, Colorado, United States

13 5. SRON Netherlands Institute for Space Research, Leiden, The Netherlands

14 6. Rocky Mountain Institute, Boulder, Colorado, United States

15 7. North Carolina State University, Raleigh, North Carolina, United States

16 8. Cooperative Institute for Research in Environmental Sciences, University of Colorado
17 Boulder, Boulder, Colorado, United States

18 9. Massachusetts Institute of Technology, Cambridge, Massachusetts, United States

19 *These authors contributed equally to the work.

20 * Correspondence to: John Worden jworden@g.ucla.edu

21

22 Abstract: Robust estimates of methane emissions are critical for understanding their impacts on
23 atmospheric warming and air quality, and for assessing methane mitigation strategies. Gridded
24 inventories, such as the U.S. Environmental Protection Agency’s Greenhouse Gas Inventory
25 (EPA GHGI), the Emissions Database for Global Atmospheric Research (EDGAR 2024), and
26 the National Oceanic and Atmospheric Administration’s Fossil Fuel Oil and Gas inventory
27 (NOAA FOG), are constructed to evaluate large-scale emission patterns and support identifying
28 emission mitigation priorities and prioritizing future measurements. However, substantial
29 differences across inventories complicate such assessments. We benchmark EPA GHGI,
30 EDGAR 2024, and NOAA FOG against flux estimates from an atmospheric inversion of
31 Greenhouse Gases Observing Satellite (GOSAT) data from 2012 to 2020 over the Contiguous
32 United States (CONUS). A key technical challenge is the heterogeneous sensitivity of satellite-
33 derived fluxes, which depends on measurement uncertainty, coverage, and inversion model
34 configuration. We account for this heterogeneity by applying an inversion operator to each

35 inventory prior to comparison with the GOSAT-based estimates. The GOSAT estimates are most
36 sensitive to oil&gas and livestock emissions; oil and gas emissions are consistent with NOAA
37 FOG (14.1 Tg CH₄ yr⁻¹ in 2015), but exceed EPA GHGI and EDGAR, particularly across Texas,
38 Oklahoma, and Louisiana. GOSAT-based livestock emissions exceed EPA GHGI and EDGAR
39 by 1–2 Tg CH₄ yr⁻¹, with the largest differences in the Midwest and California. Despite these
40 discrepancies, both activity and satellite based estimates show no observable trends from 2012 to
41 2020 in fossil and livestock emissions.

42
43

44 **1. Introduction**

45

46 All GOSAT-derived emissions and corresponding inputs/algorithms are available at
47 [<https://doi.org/10.5281/zenodo.15786798>].

48 Jupyter / python code at [<https://zenodo.org/records/16921536>] shows how to compare these
49 GOSAT derived emissions to inventories.

50

51 Methane is a potent greenhouse gas that plays a significant role in atmospheric warming
52 (Saunois et al., 2020). Methane is emitted from multiple anthropogenic sources including
53 livestock, oil and gas exploitation, manure, rice cultivation, wastewater, solid waste, and coal
54 mining, and from natural sources, particularly wetlands. Methane is also the main component of
55 natural gas, a valuable global commodity that can pose safety risks when it leaks. Accurate and
56 verifiable estimates of its emissions are essential for tracking progress and guiding effective
57 mitigation strategies, and for accounting for the economic value of energy waste (IEA, 2025;
58 World Bank, 2025). Gridded methane emission inventories, such as the gridded United States
59 Environmental Protection Agency’s Greenhouse Gas Inventory (EPA GHGI), the Emissions
60 Database for Global Atmospheric Research 2024 release (EDGAR 2024), and the National
61 Oceanic and Atmospheric Administration’s Fuel-based Oil and Gas inventory (NOAA FOG), are
62 widely used for comparing sectoral emissions, primarily at the regional scale, to atmospheric
63 data (EPA, 2021; Maasakkers et al., 2023; Crippa et al., 2020, 2024; Francoeur et al., 2021,
64 Kruskamp *et al.* 2025 <https://zenodo.org/records/16782735>). However, discrepancies in

65 how the inventories are generated, e.g. from emission factor assumptions, activity data, and/or
66 spatial proxies and resolution can result in substantial variation in both the magnitude and
67 sectoral attribution of emissions (Hristov et al. 2017; Alvarez et al., 2018; Maasakkers et al.,
68 2021; Petrescu et al. 2024; Gordon 2025). In some cases, differences between inventories can be
69 as large as the emissions themselves (Figure 1), complicating the evaluation of national and
70 regional emission trends. Verification of their underlying parameterizations is often limited by
71 spatiotemporal mismatches between empirical measurements and inventory assumptions.
72 Moreover, differences between activity-based emissions and flux estimates based on
73 observations combined with atmospheric modeling (e.g., top-down atmospheric inversions) can
74 far exceed the changes inferred from the observed growth in atmospheric methane concentrations
75 (Nisbet et al., 2019; Worden et al., 2022). As a result, tracking mitigation progress using bottom-
76 up inventories alone could be unreliable without independent observational constraints. In
77 addition to these uncertainties, emissions missing in the inventories pose another significant
78 challenge. For instance, sporadic high emitters in both fossil fuel production and waste
79 management, often caused by mechanical failures, may not be captured in traditional inventories
80 (Cusworth et al., 2020, 2024; Sherwin et al., 2024); consequently, the magnitude of these
81 emissions remains poorly understood.

82 To evaluate potential uncertainties in bottom-up inventories, top-down emissions
83 estimates derived from satellite observations, such as those from the Greenhouse Gases
84 Observing Satellite (GOSAT), provide a valuable, independent constraint. These atmospheric
85 measurements inherently capture all emissions influencing methane concentrations, including
86 unreported or underestimated sources, and therefore offer a more comprehensive view of total
87 methane emissions. However, the resulting estimates and their information content (spatial
88 resolution + uncertainties) depend strongly on the observational sampling, sensitivity of the
89 observation to the emissions, choice of a priori fluxes, and the inversion regularization.
90 Consequently, over regions with limited sampling, e.g., due to clouds or low sunlight, top-down
91 analyses have greatly reduced sensitivity to nearby emissions, so the estimates there simply
92 reflect the *a priori*. In contrast, emissions inferred for regions with ample sampling are more
93 likely to accurately represent local sources. The focus of this paper is to demonstrate how this
94 GOSAT-based benchmark can be used to evaluate alternative gridded inventories while
95 accounting for its variable information content as discussed next.

97 **Method and Data**

98 **Accounting for choice of *a priori* and inversion regularization:** Comparisons between
 99 satellite-based top-down fluxes and activity-based inventories must account for the variation in
 100 sensitivity of the data to emissions and choice of *a priori*, otherwise substantial uncertainty (also
 101 known as *smoothing error*) is introduced into the comparison (Rodgers, 2000; Worden et al.,
 102 2022, 2023). Smoothing error in this context can be mitigated for these comparisons by at least
 103 three ways: 1) by using the inventory as the *a priori* in the inversion or 2) by applying an
 104 inversion operator to the inventory being compared (the inversion operator depends on the
 105 inversion *a priori* and what is called the averaging kernel matrix, Appendix B) or 3) by adjusting
 106 the GOSAT based estimate using the gridded inventory and the averaging kernel matrix to
 107 replace the effect of the original prior (also known as prior swapping).

108 In the first scenario, recalculating the inversion and subsequently comparing to the *a*
 109 *priori* is computationally expensive (e.g., Nesser et al., 2024 and references therein) as it
 110 involves minimizing a cost function of gridded emissions vector (e.g. \mathbf{z}) that typically has the
 111 following form:

$$112 \quad \mathbf{C} = \|\mathbf{y} - \mathbf{F}(\mathbf{z}_A)\|_{\mathbf{S}_n^{-1}}^2 + \|\mathbf{z} - \mathbf{z}_A\|_{\mathbf{S}_A^{-1}}^2 \quad (1)$$

113 Where \mathbf{y} is a state vector representing concentrations (e.g. total column methane or XCH_4), the
 114 forward model $\mathbf{F}(\mathbf{z}_A)$ in this case is the Goddard Earth Observing System – Chemistry model
 115 (GEOS-Chem) driven by a distribution of *a priori* emissions (\mathbf{z}_A). The matrix \mathbf{S}_n represents the
 116 measurement error covariance for the total column data and the matrix \mathbf{S}_A represents the
 117 uncertainty (or covariance) in our *a priori* emissions. For the benchmark described in this paper,
 118 the vector \mathbf{z} represents the spatial distribution of anthropogenic emissions by sector, in this case
 119 livestock, waste, coal, rice, oil&gas. Wetlands and fire emissions are also estimated with the
 120 GOSAT data and the effect of jointly estimating these emissions are included in the posterior
 121 covariance and uncertainties of the anthropogenic emissions estimate (Worden *et al.* 2022;
 122 2023).

123 The estimate for the converged solution, $\hat{\mathbf{z}}$, can be related to the “true distribution” of the
124 emissions (\mathbf{z}) with the following (e.g. Rodgers 2000).

$$125 \quad \hat{\mathbf{z}} = \mathbf{z}_A + \mathbf{A}(\mathbf{z} - \mathbf{z}_A) \quad (2)$$

126
127 where for clarity we have not included the uncertainty terms (see Appendix B). The averaging
128 kernel matrix \mathbf{A} is a function of the *a priori* and posterior covariance, $\hat{\mathbf{Z}}$ and \mathbf{Z}_A (see Appendix B
129 for a description of uncertainties and prior covariances) and describes the sensitivity of the
130 distribution of estimated emissions to the true state ($\mathbf{A} = \frac{\partial \hat{\mathbf{z}}}{\partial \mathbf{z}}$). Approach #2, which is to apply an
131 inversion operator to the inventory, is equivalent to replacing \mathbf{z} , or the “true distribution” of
132 emissions, with the alternative inventory, \mathbf{z}_I in Equation 1; this approach is commonly used for
133 data assimilation or for comparing atmospheric trace gas profiles from models or in situ
134 measurements to remotely sensed measurements (e.g. Wecht *et al.* 2014, Herman *et al.* 2014).
135 This revised estimate can be compared to $\hat{\mathbf{z}}$ while accounting for the *a priori* and regularization
136 choices made in the inversion described by Equation 1. Approach #3 (or prior swapping) instead
137 involves replacing \mathbf{z}_A with the alternative inventory (e.g. Rodgers and Connor 2003)

$$138 \quad \hat{\mathbf{z}}_{new} = \hat{\mathbf{z}} - (\mathbf{I} - \mathbf{A})\mathbf{z}_A + (\mathbf{I} - \mathbf{A})\mathbf{z}_I \quad (3)$$

140 And is equivalent to re-running the inversion described by Equation (1) with this alternative *a*
141 *priori*.

142 As approaches 2 and 3 are linear operations, they result in equivalent comparative differences as
143 shown in Appendix B. In this manuscript we use the inversion operator approach (Equation 2)
144 for consistency with previous publications (e.g. Worden *et al.* 2022; 2023).

145 **Sector Based Attribution:** We use estimates of gridded integrated fluxes from a GEOS-Chem
146 based inversion using GOSAT XCH₄ data as described in Qu *et al.* (2022,2024). We use a
147 Bayesian-based sectoral partitioning approach (Appendix A, Worden *et al.*, 2022, 2023) to
148 project these top-down integrated fluxes to emissions by sector at a 1° × 1° resolution. This
149 approach characterizes the inversion solution by providing a posterior covariance for the solution
150 and provides the “inversion operator” (Equation 2) that, when applied to a gridded inventory,

151 enables the comparison to inversion results by capturing the influence of the inversion’s prior
152 emissions and the sensitivity of the satellite observations to those emissions (Rodgers, 2000).

153
154 **Inventories:** (See Appendix C for more detail) The inventories we compare include EDGAR
155 2024 (Crippa et al. 2024), the gridded U.S. EPA GHG inventory (GHGI) (Maasakkers et al.
156 2023), and NOAA FOG (Francoeur et al. 2021). The EDGAR and GHGI inventories provide
157 information about methane emissions across multiple sectors (e.g., livestock, waste, oil and gas,
158 coal, rice). The approaches estimating these emissions vary, with EDGAR down-scaling national
159 totals to finer scales using spatial information about the sources using global datasets while the
160 GHGI gridded inventory reflects emission factors and activity data used in the EPA U.S.
161 Greenhouse Gas Inventory. In contrast, NOAA FOG focuses specifically on fossil methane
162 emissions and is a hybrid inventory that integrates atmospheric CH₄ and NO₂ observations with
163 activity-based NO₂ metrics (Francoeur et al. 2021). While these inventories show considerable
164 overlap in the location of emissions, differences can be large, even when aggregating from the
165 original 0.1 degree grid of the inventories to the 1 degree grid shown for Figure 1.

166
167 As stated previously, our goal for this study is to demonstrate a benchmark for U.S.
168 methane emission gridded inventories and their changes from 2012 to 2020. These comparisons
169 are documented and publicly accessible at Zenodo (see data availability); Jupyter notebooks are
170 provided here that demonstrate how to compare gridded inventories to GOSAT-based emissions.
171 These benchmarks will be updated as newer datasets, such as inverse analyses using Sentinel-5P
172 TROPOMI (Tropospheric Ozone Monitoring Instrument) observations, become available (e.g.,
173 Nesser et al. 2024; Hancock et al. 2025). Readers unfamiliar with the Bayesian attribution
174 framework, the GOSAT inversion, or the specific inventories compared are encouraged to
175 consult the appendices, where these methods are summarized, or our previously published work
176 on the subject (Cusworth et al. 2021; Worden et al. 2022,2023).

177

178 **2. Integrated total and sectoral USA emissions for 2015**

179

180 Table 1 summarizes U.S. methane emissions by sector for 2015, based on the GOSAT
 181 data and the sectoral attribution approach described in this study (Appendix A). The error
 182 characterization (Appendix B) includes uncertainties from the *a priori* as well as measurement
 183 and model systematic error. The prior emissions are taken from Worden *et al.* (2023). Table 1
 184 also shows a quantity called the Degrees of Freedom for Signal (DOFS), which is given by the
 185 trace of the averaging-kernel matrix for the corresponding state-vector elements in \mathbf{z} . The DOFS
 186 describe the extent to which the estimate is informed by observations rather than prior
 187 assumptions (Appendix B), as well as the spatial information content. For example, from
 188 Equation 2, if $\mathbf{A} \approx \mathbf{0}$ (equivalent to DOFS = 0), observations say essentially nothing about the
 189 emissions and the estimate reduces to the prior. If \mathbf{A} is the identity matrix, then the DOFS equals
 190 the number of state-vector elements and the estimate exactly reflects the true distribution,
 191 modified by the expected uncertainties (Appendix B). The DOFS reported in Table 1 refer to the
 192 spatially distributed estimate, not for the total emissions value. Hence, DOFS > 1 means there is
 193 at least some spatial information for that sector's estimate.

194 For this GOSAT-based benchmark, the highest information content is available for total,
 195 livestock, and oil and gas (O&G) emissions, while waste emissions estimates are only
 196 moderately constrained by the data, and rice and coal emissions have limited observational
 197 information. This variability in information content underscores the need for careful
 198 interpretation of top-down estimates, particularly when examining spatial and sectoral patterns or
 199 trends.

200

201 Table 1: GOSAT-Based CONUS Anthropogenic Emissions and Information Content by
 202 Sector (2015)

Sector	Emissions (Tg CH₄/yr)	<i>A priori</i> (Tg CH₄/yr)	DOFS*
Total	29.4 ± 1.5	28.2±2.0	3.4
Livestock	10.3 ± 1.2	9.2 ± 1.4	1.8
Rice	0.4 ± 0.1	0.4±0.1	0.0
Waste	4.5 ± 0.6	5.6±0.8	0.6
Oil & Gas	11.1 ± 0.9	9.9±1.2	1.0

Coal 3.1 ± 0.3 3.1 ± 0.3 0.1

203

204 Table 2 compares our emissions to previous inversions using atmospheric data and to the
 205 inventories discussed in this paper (Appendix C). As can be seen in Table 2, our atmospheric-
 206 based emissions are generally consistent with other studies, typically within 1–2 standard
 207 deviations of the reported uncertainties, even though each study uses different priors, has
 208 different systematic errors, and has different sensitivity to the underlying emissions. These
 209 comparisons also show that total emissions from atmospheric-based inversions are typically
 210 larger than activity-based estimates, with the livestock and oil and gas sectors responsible for
 211 most of the discrepancy.

212

213

214 Table 2: Comparison of Methane Emissions by Study. All totals are CONUS

215 anthropogenic; years as listed;

216 *(All values in Tg CH₄/yr)*

Study	Total	Livestock	Rice	Waste	Oil & Gas	Coal
(Atmospheric Inversions)						
GOSAT (2015 This Work)	29.4 ± 1.5	10.4 ± 1.2	0.4 ± 0.1	4.6 ± 0.6	11.1 ± 0.9	3.1 ± 0.3
GOSAT (2019)¹	27.3 ± 3	9.9 ± 0.9	0.3 ± 0.1	4.0 ± 0.7	10.3 ± 1.0	2.8 ± 0.4
TROPOMI (2019)²	30.9 ± 0.9	10.4 ± 0.3	N/A	6.9 ± 0.6	10.4 ± 0.3	1.5 ± 0.4
GOSAT + Surface (2009– 2020)³	29.1 ± 0.5	8.8 ± 0.3	N/A	4.2 ± 0.1	14.1 ± 0.2	2 ± 0.4
GOSAT (2010–2015)⁴	31 ± 1.0	9.4 ± 0.4	0.4 ± 0.2	6.2 ± 0.2	11.1 ± 0.6	3.2 ± 0.1
In Situ (2007-2008)⁵	33.4 ± 2	N/A	N/A	N/A	N/A	N/A
In Situ (2003)⁶	32.4 ± 5	N/A	N/A	N/A	N/A	N/A
(Activity Models and Year)						
GHGI (2015)⁷	23.7 ± 2.1	8.9 ± 1.4	0.6 ± 0.3	4.8 ± 1.4	6.9 ± 1	2.5 ± 0.4
EDGAR (2015)⁸	25.7 ± 2.1	8.6 ± 1.4	0.3 ± 0.1	4.3 ± 1.3	10.1 ± 1	2.4 ± 0.4

217
218 **Table 2: Comparison of Methane Emissions by Study.** All totals are CONUS anthropogenic
219 emissions for the years listed. Values are reported in Tg CH₄ yr⁻¹. Atmospheric inversions
220 exclude natural sources and fire emissions where sectoral separation is available. Activity-based
221 estimates include the gridded EPA GHGI, EDGAR 2024, and NOAA FOG inventories evaluated
222 in this study. References: (1) Worden et al. (2022), (2) Nesser et al. (2024), (3) Janardanan et al.
223 (2024), (4) Maasakkers et al. (2019), (5) Miller et al. (2013), (6) Kort et al. (2008), (7)
224 Maasakkers et al. (2016, 2023), (8) Crippa et al. (2024), and (9) Francoeur et al. (2021).

225

226

227 *2.1 Oil and Gas Emissions (GOSAT, FOG, EPA, and EDGAR)*

228

229 We next compare the GOSAT-based emissions for O&G to those from NOAA FOG,
230 GHGI, and EDGAR inventories. In particular, we demonstrate how applying the inversion
231 operator to these inventories modifies our interpretation of the comparison.

232

233 **Spatial Distribution for 2015:** Figures 2 through 4 compare the spatial distribution of U.S. oil
234 and gas (O&G) methane emissions in 2015 from the GOSAT inversion with those from the
235 FOG, GHGI, and EDGAR (2024 release, Crippa et al., 2024) inventories respectively. These
236 comparisons demonstrate the importance of accounting for the varying information content of
237 the GOSAT inversion, which is influenced by both the prior emissions used in the inversion and
238 the sensitivity of the aggregated satellite observations to underlying emission patterns (Worden
239 et al., 2023 and references therein). In Figure 2, the upper left panel (a) shows the GOSAT based
240 estimate. The upper right panel (b) shows the original FOG emissions. The middle left panel (c)
241 shows the difference between the top two. The middle right panel shows the difference between
242 FOG emissions and GOSAT based emissions after applying the inversion operator (denoted
243 AK). All figures use 1x1 degree gridding. The bottom right panel (E) shows the diagonal of the
244 averaging kernel (or DOFS) corresponding to that location for oil and gas emissions. As seen in
245 the left panel of Figure 2, significant regional discrepancies between the GOSAT and FOG
246 inventories exist, with similar magnitude differences as shown in Figure 1. However, after

247 applying the inversion operator (Equation 2) to the FOG inventory (labeled FOG AK), many of
248 these differences are greatly reduced (middle right panel)

249 Small differences between GOSAT and the inventory, after applying the inversion operator, can
250 also occur because of limited sensitivity, as indicated by the DOFS, for example over the Bakken
251 region of North Dakota. As discussed previously and shown in Equation 2 and Appendix B, in
252 such cases the difference between the GOSAT estimate and the inventory adjusted by the
253 inversion operator should be close to zero, because both terms reduce to $\sim Z_A$. In contrast, the
254 GOSAT estimate shows increased sensitivity to emissions in Oklahoma, Texas, and Louisiana.
255 Based on this comparison, and on the integrated total emissions in the next section, we conclude
256 that the GOSAT estimate does not falsify the spatial distribution of methane emissions posited
257 by the FOG oil and gas inventory.

258

259 **Interpreting Comparisons between GOSAT, EDGAR, and GHGI emissions:**

260

261 Comparisons between GOSAT and EDGAR (Figure 3) and between GOSAT and EPA GHGI
262 (Figure 4) show larger discrepancies, even after applying the inversion operator, particularly in
263 northwest Colorado, Texas, Oklahoma, and Louisiana. These patterns indicate substantial
264 inventory uncertainties in well-observed regions with intensive oil and gas activity. Some
265 regions are sparsely observed by GOSAT, so their contributions may be important but their
266 uncertainties cannot be reliably assessed with this benchmark. When measurement cost is a
267 constraint, the discrepancy hotspots identified here are high-value targets for additional
268 observations, with expanded coverage of under-sampled regions as resources allow.

269

270 Previous studies (e.g., Alvarez et al. 2018; Cusworth et al. 2022; Sherwin et al., 2024)
271 have shown that a small number of high emitters (e.g., <2%; Sherwin et al., 2024), likely due to
272 unplanned mechanical failures, contribute disproportionately to the fossil methane budget. These
273 sources are likely underrepresented or missing from activity-based inventories. The agreement
274 between FOG and GOSAT supports this conclusion, as the FOG inventory integrates
275 atmospheric CH₄ with NO_x observations and activity metrics; these regional CH₄ observations
276 capture emissions under-represented in purely bottom-up approaches. If such super-emitters are

277 entirely responsible for the discrepancies between GOSAT and the EPA GHGI and EDGAR
278 inventories, then comparisons between the GOSAT, EPA, EDGAR, and FOG O&G emissions in
279 Table 2 suggest these sources are undercounted by ~ 7 Tg CH₄/yr of reported natural gas
280 emissions, far exceeding previous estimates, as previously documented in other studies (e.g.,
281 Alvarez et al. 2018; Cusworth et al. 2022; Sherwin et al., 2024; Zavala-Araiza et al. 2015).

282
283

284 **Integrated totals for 2015:** Figure 5 compares integrated total oil and gas (O&G) emissions
285 derived from GOSAT with those from the FOG, GHGI, and EDGAR inventories.

286 Before applying the inversion operator, total FOG emissions are estimated at 14.1 ± 2 Tg CH₄
287 yr⁻¹. We assumed the same prior covariance structure (\mathbf{Z}_A , Appendix B; Worden et al., 2022,
288 2023) for FOG as for the GOSAT *a priori*. This yields a smaller total uncertainty (2 Tg CH₄ yr⁻¹)
289 than the ~ 2.8 Tg CH₄ yr⁻¹ uncertainty for total FOG O&G emissions inferred from a Monte Carlo
290 analysis of NO_x activity data (Francoeur *et al.*, 2021). Using a different covariance structure that
291 is consistent with the stated uncertainty in total emissions could therefore change conclusions
292 about whether the GOSAT estimate falsifies the FOG inventory, and the inversion-operator
293 methodology in Equation 2 would allow this. However, a full covariance is required, with
294 explicitly computed off-diagonal terms such that, when projected to a single number, it
295 reproduces the expected uncertainty reported in, for example, Francoeur et al. (2022).

296 After applying the inversion operator, the FOG total is reduced to 11.4 Tg CH₄ yr⁻¹. The
297 uncertainty shown for the modified FOG estimate (denoted FOG-AK) reflects the uncertainty in
298 the difference between the GOSAT-based estimate and the FOG-AK estimate (Appendix B
299 Equation 15), not the uncertainty of the FOG-AK estimate itself. Because the FOG-AK estimate
300 is consistent with the GOSAT-based inversion within the reported uncertainty, this comparison
301 suggests that the GOSAT estimate does not falsify the original, higher FOG total of 14.1 Tg CH₄
302 yr⁻¹.

303 Figure 5 also shows comparisons to GHGI and EDGAR. For these inventories, uncertainties
304 prior to applying the inversion operator are derived using the same prior covariance structure as
305 for the GOSAT a priori, because published full covariances are not readily available.

306 In contrast to the FOG comparison, both the EPA and EDGAR estimates, with or without
307 application of the inversion operator, are inconsistent with the GOSAT-based inversion. Their
308 differences lie well outside the post-operator uncertainty shown for each inventory. As shown in
309 Figures 3 and 4 these differences are spatially located primarily in the Texas, Oklahoma, and
310 Louisiana regions. As noted previously, additional measurements here are therefore likely to
311 reduce uncertainties in the USA O&G methane budget.

312
313 **Integrated Totals: 2012–2020:** Figure 6 shows annual methane emissions from 2012 to 2020.
314 Despite substantial increases in oil and gas production over this period, all gridded inventories
315 and the GOSAT top-down estimates show no significant change in total U.S. methane emissions,
316 although the FOG inventory may have a slight increase. This apparent disconnect between rising
317 production and stable emissions has been noted in several studies and is commonly attributed to
318 improvements in production efficiency, leak detection, and emissions control technologies (e.g.,
319 Lu et al., 2023). EPA GHGI supports this conclusion, showing relatively flat changes in fossil
320 fuel methane emissions over the same period. This stability in the activity estimate is explained
321 by offsetting trends, including a decline in exploration emissions due to fewer well completions,
322 the adoption of lower-emitting equipment, and stable or slightly declining well counts
323 (Maasakkers et al. 2023). For instance, while natural gas production increased by 26% and crude
324 oil production by 67%, the number of active gas and oil wells remained roughly constant,
325 declining slightly over the period. Emissions from gas systems were flat overall, with increases
326 in gathering and boosting offset by decreases in production and processing. Similarly, petroleum
327 system emissions rose by just 11% due to a significant drop in exploration-related emissions
328 (Maasakkers et al. 2023).

329
330 *2.2 Livestock Emissions (GHGI and EDGAR)*
331

332 **Spatial Distribution for 2015:** Similar to Figures 2-4, Figures 7 and 8 show the spatial
333 distribution of livestock methane emissions from GOSAT, EDGAR, and GHGI data. The FOG
334 inventory is limited to oil and gas emissions and is therefore excluded from this and subsequent
335 comparisons. Methane emissions from livestock generally scale with herd size, particularly dairy
336 and beef cattle. Dairy cows typically emit more than twice as much methane as beef cows, due to
337 higher enteric fermentation (Wolf et al., 2017; Hristov et al., 2017). Emissions vary
338 geographically with management and environmental conditions (for example grazing
339 practices, feed quality, and temperature, Wolf et al., 2017). Inventories account for this
340 using region-specific emission factors, but if the factors used are not representative of
341 actual local conditions, the resulting difference between the atmospheric based and activity
342 based emissions should be spatially structured rather than random. Consistent with this,
343 we observe systematic regional biases relative to the GOSAT-based estimates: inventories
344 in California and the northern states are higher than GOSAT, whereas inventories in
345 northern Texas are lower.

346
347 **Integrated Total for 2015:** Figure 9 compares integrated livestock methane emissions from
348 GOSAT with GHGI and EDGAR inventories, each shown with and without the inversion
349 operator applied. The GHGI and EDGAR totals differ modestly. The EPA total lies slightly
350 outside the GOSAT uncertainty range, while the EDGAR total falls within it. However,
351 agreement in totals does not imply agreement in spatial patterns. For EDGAR in particular,
352 closer total agreement with GOSAT coincides with offsetting regional deviations, with positive
353 differences in parts of the Midwest and negative differences in California. These cancellations
354 reduce the apparent mismatch in the national total, which underscores the importance of
355 evaluating spatial variability alongside integrated totals. Overall, comparisons of integrated
356 totals and spatial patterns indicate substantial remaining uncertainty in livestock emissions.
357 Additional measurements over California and the Midwest, especially in the Texas and
358 Oklahoma region, would likely reduce this uncertainty.

359
360 **Integrated Totals for 2012-2020:** Figure 10 (and Table 2) shows comparisons between the
361 integrated total livestock emissions from the GOSAT based inversion and the GHGI and
362 EDGAR inventories. The GOSAT-based estimate as well as those from the GHGI and EDGAR

363 inventories do not observably change within the calculated uncertainties, except possibly for the
364 year 2019. We therefore conclude that GOSAT based livestock emissions cannot falsify the
365 posited (flat) trends from activity data (Maasakkers et al. 2021).

366

367 2.3 Waste (GHGI and EDGAR)

368 Figures 11 and 12 show the spatial distribution of methane emissions from the waste
369 sector based on GOSAT, GHGI, and EDGAR estimates and Figure 13 shows the integrated total
370 for 2015. The largest differences are for California for the EDGAR / GOSAT comparison. The
371 integrated waste sector methane emissions from GOSAT are estimated at 4.5 ± 0.6 Tg CH₄/yr,
372 while both GHGI and EDGAR report lower values of 4.2 ± 0.3 Tg CH₄/yr. These differences are
373 not statistically significant, as the GOSAT estimate lies within the uncertainty range of both
374 inventories (after applying the inversion operator). However, there is very limited spatial
375 information content in the GOSAT waste estimate (~0.6 DOFS total). Consequently, the spatial
376 differences shown in the right-bottom panel don't show meaningful differences between the
377 inventories and the GOSAT waste estimate for most of the country. Because of this limited
378 sensitivity we do not compare temporal changes in the waste emissions.

379

380 3. Summary and Future Directions

381

382 Top-down methane emissions estimates vary in their information content depending on
383 the emission sector and observing system. For these GOSAT based emissions estimates,
384 information content is greatest for oil and gas and livestock, so these sectors are best suited for
385 inventory evaluation using the results shown here. Waste, coal, and rice exhibit lower
386 information content in this analysis because GOSAT does not adequately sample methane
387 variability attributable to those sources. Even so, our information-content-based comparison
388 identifies where additional measurements would yield the largest uncertainty reductions in
389 gridded inventories.

390 In particular, our results highlight the need for targeted measurement campaigns,
391 especially in the Texas, Oklahoma, and Louisiana drilling basins, where additional data can most
392 effectively reduce inventory uncertainties. For the livestock sector, California and Northern

393 Texas stands out as key regions where improved activity based and atmospheric methane
394 observation can have the highest impact. These findings underscore the importance of
395 prioritizing high-emitting or uncertain regions to refine national methane budgets.
396 Beyond regional targeting, improving inversion resolution is also key. Higher-resolution flux
397 estimates, whether through satellites like TROPOMI or plume-resolving instruments (e.g., Jacob
398 et al. 2022; Pandey et al. 2025 and refs therein), are particularly needed for sectors such as waste,
399 coal, and oil and gas, where coarse-resolution inversions struggle to isolate source signals. In
400 particular, integrating plume-resolving and area-flux estimates enhances the sectoral attribution
401 of emissions and improves the information content for inventory evaluation (Pandey *et al.* 2025).

402

403 **(Trends)** Inversions conducted using GOSAT data and GEOS-Chem (see references in
404 Table 2), show no discernible trend over the analysis period, which is consistent with all three
405 gridded inventories discussed in this manuscript. However, the fact that other inversions show
406 different trends highlights the importance of benchmarking approaches (Janardanan et al. 2024),
407 not only for validating inventories but also for identifying uncertainties in inversion outputs
408 themselves. These differences matter for informing effective remediation strategies and setting
409 realistic expectations for emission reductions.

410 As satellite constellations improve in spatial resolution, sampling, and accuracy, top-
411 down flux estimates become more accurate at higher spatial resolution (e.g., Jacob et al., 2022).
412 Using TROPOMI, Nesser et al. (2024) produced a 2019 North American emissions map with a
413 degree of freedom for signal (DOFS) of ~ 772 , more than two orders of magnitude higher than in
414 our GOSAT record, driven by a similar increase in observations. This resolution enables explicit
415 estimation of many large sources, including landfills. East et al. (2025) extended this approach to
416 global coverage at similar ~ 25 km gridding. Building a benchmark from the combined record
417 will help evaluate how countries have managed emissions before and after the Global Methane
418 Pledge, which targets a 30 percent reduction from 2020 to 2030. Our approach shows how
419 inventories can be benchmarked against these improved flux estimates to reduce uncertainty,
420 especially smoothing error, without re-running inversions with inventory priors. Combining
421 high-resolution, independent datasets will support more accurate methane inventories, clarify
422 source trends, and inform effective mitigation strategies.

423 **Appendices**

424 **Appendix A: GOSAT Methane Fluxes and Projection to USA Emissions by Sector**

425 **(Overview)** Yearly sectoral emissions by region based on the satellite data are generated in a two
426 step process. The first step is to quantify global integrated fluxes using total atmospheric column
427 methane data from the Japanese GOSAT (Greenhouse gases Observing SATellite) instrument
428 (Parker *et al.* 2011) and the GEOS-Chem model (Zhang *et al.*, 2021). The approach used to
429 generate fluxes has been extensively documented in past literature (e.g. Zhang *et al.*, 2021, Qu *et*
430 *al.*, 2024), and we refer the reader to these articles. The state vector for this inversion include 1)
431 yearly anthropogenic methane emissions between 2010 and 2022 at a gridding of 5x4 degrees
432 (longitude/latitude) and we use the estimates between 2012 and 2020 for this study, 2) wetland
433 methane emissions for specified regions for each month between 2010 to 2022), and 3) the
434 yearly hemispheric methane sink. The second step (next section) is a linear estimate based on an
435 optimal estimation sectoral emissions attribution approach (Cusworth *et al.* 2021; Worden *et al.*
436 2022) that projects the integrated anthropogenic fluxes to emissions by sector and trends at the
437 same 5x4 degree gridding and then again at 1x1 degree (lon/lat) gridding over the USA. This
438 projection accounts for the prior distribution and uncertainties in the emissions (e.g. Worden *et*
439 *al.* 2022). We next provide more detail on projection/attribution methodology as it is relevant to
440 the benchmarking methodology that is the focus of this paper.

441 **(Sectoral attribution of fluxes to emissions)** We use a Bayesian based approach to project the
442 fluxes described in the previous section (at 5x4 degrees lon/lat) to emissions by sector at 1x1
443 degree. The full methodology is described in Cusworth *et al.* (2021) and first applied to methane
444 fluxes in Worden *et al.* (2022) and again in Worden *et al.* (2023). This approach is equivalent to
445 swapping the *a priori* assumptions, given by \mathbf{x}_A and \mathbf{S}_A , to a different state vector \mathbf{z}_A (and *a priori*
446 covariance \mathbf{Z}_A) when a linear relationship between the different state vectors \mathbf{x} and \mathbf{z} exist. The
447 approach provides the full posterior and prior covariances and priors needed to account for the
448 varying information content of satellite based emissions estimates when comparing these
449 emissions to either each other (e.g. between years) or to inventories (Worden *et al.* 2023) or to
450 other estimates. We refer the reader to these papers, starting with Cusworth *et al.* (2021) for the
451 primary derivation, and summarize here.

452

453 Given a linear mapping between one state vector and another (e.g. between fluxes \mathbf{x} at 5x4
454 degrees versus emissions \mathbf{z} at 5x4 degrees or alternatively emissions at 1x1 degree):

455

$$456 \quad \mathbf{x} = \mathbf{M}\mathbf{z}, \quad (4)$$

457

458 As discussed in Worden et al. (2023), the solution for projecting fluxes back to emissions takes
459 the form:

460

$$461 \quad \hat{\mathbf{z}} = \mathbf{z}_A + \hat{\mathbf{Z}}\mathbf{M}^T\hat{\mathbf{S}}^{-1}[(\mathbf{I} - \hat{\mathbf{S}}\mathbf{S}_A^{-1})(\mathbf{x}_A - \mathbf{M}\mathbf{z}_A) + (\hat{\mathbf{x}} - \mathbf{x}_A)] \quad (5)$$

462

463 where the $\hat{\mathbf{z}}$ and \mathbf{z}_A is the posterior and prior emissions state vector respectively with posterior
464 and prior error covariance $\hat{\mathbf{Z}}$, \mathbf{Z}_A respectively.

465

466 The posterior emission error covariance matrix $\hat{\mathbf{Z}}$ is calculated explicitly given \mathbf{M} , \mathbf{S}_A , $\hat{\mathbf{S}}$, and
467 prior emissions error covariance matrix \mathbf{Z}_A :

468

$$469 \quad \hat{\mathbf{Z}} = (\mathbf{M}^T(\hat{\mathbf{S}}^{-1} - \mathbf{S}_A^{-1})\mathbf{M} + \mathbf{Z}_A^{-1})^{-1} \quad (6)$$

470

471

472 Here, the $\hat{\mathbf{S}}$ is the posterior covariance for the fluxes described in the Qu *et al.* (2024), with prior
473 error covariance \mathbf{S}_A , given as a diagonal matrix with values of 0.5 (squared). The \mathbf{I} is the identity
474 matrix. The prior covariances for each emission category (livestock, waste, rice, coal, oil and
475 gas, and fires) are described in Worden et al. (2022) and Worden et al. (2023).

476

477

478 ***Uncertainty Calculation***

479

480 After projecting the estimate for integrated fluxes at 5x4 degrees ($\hat{\mathbf{x}}$) to emissions by sector at
 481 1x1 degree ($\hat{\mathbf{z}}$), we can describe $\hat{\mathbf{z}}$ using Equation 2 with corresponding averaging kernel as
 482 discussed in the introduction (and now including uncertainties):

$$483$$

$$484 \hat{\mathbf{z}} = \mathbf{z}_A + \mathbf{A}(\mathbf{z} - \mathbf{z}_A) + \boldsymbol{\delta}_n + \boldsymbol{\delta}_m \quad (7)$$

485
 486 where $\boldsymbol{\delta}_n$ and $\boldsymbol{\delta}_m$ are the errors from measurement error and model error respectively. The
 487 measurement and model errors are discussed in Worden *et al.* (2022, 2023). The error
 488 covariance for $\hat{\mathbf{z}}$ is then given by:

$$489$$

$$490 E\|\hat{\mathbf{z}} - \mathbf{z}\|^2 = \mathbf{Z}_{\text{total}} = (\mathbf{I} - \mathbf{A})\mathbf{Z}_A(\mathbf{I} - \mathbf{A})^T + \mathbf{S}_n + \mathbf{S}_m \quad (8)$$

491
 492 Note that the inverse of the Hessian (Equation 6) is equivalent to the first two terms (Worden *et al.*
 493 *et al.* 2004; Bowman *et al.* 2006):

$$494$$

$$495 \hat{\mathbf{Z}} = (\mathbf{I} - \mathbf{A})\mathbf{Z}_A(\mathbf{I} - \mathbf{A})^T + \mathbf{S}_n \quad (9)$$

496
 497 Equation 9 allows us to separate the “smoothing error” (the first term on the RHS of Equation 9),
 498 from the measurement error in order to better evaluate comparisons between the GOSAT and
 499 inventory methane estimates as discussed in the next section.

500
 501 In order to calculate the emissions for either a region (e.g. USA) or a category of emissions (e.g.
 502 rice), we must first sum the corresponding elements of the state vector:

$$503$$

$$504$$

$$505 \mathbf{z}_i = \mathbf{h}_i \hat{\mathbf{z}}, \quad (10)$$

506
 507 Where \mathbf{h}_i is a column vector that projects the desired elements of $\hat{\mathbf{z}}$ to region or sector i , \mathbf{z}_i . As
 508 discussed in Worden *et al.* (2022), the uncertainty of \mathbf{z}_i is then given by

$$509$$

$$510 \sigma_i^2 = \mathbf{h}_i \mathbf{Z}_{\text{total}} \mathbf{h}_i^T \quad (11)$$

511
512
513
514
515
516

As discussed in these previous papers, this uncertainty calculation accounts for the effects of cross-terms (e.g. wetlands, OH, fires). Equation (11) is what is used to calculate the uncertainties shown in the figures and the tables in this paper.

517 **Appendix B: Bayesian / Optimal Estimation Approach for Comparing Inventory to top-** 518 **down Inversion**

519 To compare a $0.1^\circ \times 0.1^\circ$ inventory with top-down fluxes based on an inversion of atmospheric
520 data, we first project the inventory to the same spatial scale as the top-down fluxes and then
521 account for the sensitivity of the top-down estimates. The native resolution of the gridded
522 inventories is 0.1° , provided by sector. In contrast, the GOSAT based fluxes are at a coarser
523 resolution of $5^\circ \times 4^\circ$ (longitude \times latitude) and represent integrated fluxes (Qu et al., 2024) with
524 no sectoral specificity in each grid. Our approach is to first re-grid the inventory to $1^\circ \times 1^\circ$, while
525 retaining sectoral distinctions (e.g., livestock, waste, rice, coal, oil & gas). As discussed in the
526 following paragraph, we then project the $5^\circ \times 4^\circ$ GOSAT-inverted methane fluxes to sector-
527 specific emissions at $1^\circ \times 1^\circ$ resolution as discussed in Appendix A. We selected this
528 intermediate resolution to better represent national emission patterns, as a $5^\circ \times 4^\circ$ grid can cause
529 significant overlapping flux contributions from neighboring countries such as the United States,
530 Canada, and Mexico.

531
532 The comparison approach is described in Worden *et al.* (2023) and summarized here. We next
533 project the inventory (\mathbf{z}_i) through the “inversion operator” (Equation 2) in order to account for
534 the choice of a priori in the inversion and the sensitivity of the emissions (Rodgers 2000, Worden
535 *et al.* 2022, 2023).

$$536 \quad 537 \quad \hat{\mathbf{z}}_i = \mathbf{z}_A + \mathbf{A}(\mathbf{z}_i - \mathbf{z}_A) \quad (12)$$

538

539 Where \mathbf{z}_A is a vector describing the *a priori* methane emissions used for the top-down estimate
 540 and \mathbf{A} is the averaging kernel matrix calculated for that inversion. The averaging kernel matrix is
 541 a function of the prior and posterior covariance, $\hat{\mathbf{Z}}$ and \mathbf{Z}_A :

$$543 \quad \mathbf{A} = \mathbf{I} - \hat{\mathbf{Z}}\mathbf{Z}_A^{-1} \quad (13)$$

544
 545 The DOFS shown in Table 1 are calculated by taking the sum of diagonal elements (or trace) of
 546 the averaging kernel corresponding to the sector.

547
 548 After application of the inversion operator a comparison of these modified inventory emissions
 549 with the GOSAT- based emissions (Cusworth et al. 2021, Worden et al. 2023, Appendix A) is
 550 given by:

$$552 \quad \hat{\mathbf{z}} - \hat{\mathbf{z}}_i = \mathbf{A}(\boldsymbol{\delta}_i) + \boldsymbol{\delta}_n + \boldsymbol{\delta}_m \quad (14)$$

553
 554 Where $\boldsymbol{\delta}_i$ is the uncertainty in the inventory, $\boldsymbol{\delta}_n$ is the uncertainty in the inversely estimated
 555 emissions due to noise in the atmospheric data, and $\boldsymbol{\delta}_m$ is the uncertainty in the model used to
 556 project concentrations to emissions. The effect of the prior, \mathbf{z}_A , is also removed in this
 557 comparison described by Equation 14 so that the inventory can be compared to the satellite based
 558 emissions without this large effect of smoothing error on the comparison (see subsequent figures
 559 and supplemental). The error of the difference between satellite estimate and this adjusted
 560 inventory is then the expectation of the difference:

$$563 \quad E\|\hat{\mathbf{z}} - \hat{\mathbf{z}}_i\| = \mathbf{A}\mathbf{S}_i\mathbf{A}^T + \mathbf{S}_n + \mathbf{S}_m \quad (15)$$

564
 565 Where \mathbf{S}_i is the covariance for the inventory uncertainties $\boldsymbol{\delta}_i$, \mathbf{S}_n is the measurement error
 566 projected to emissions, and \mathbf{S}_m is the model error. Note that \mathbf{S}_n is directly calculated from the
 567 inversion (Worden et al. 2023). The final term in Equation 15, the model error, can be highly
 568 challenging to quantify. Previous studies have pointed towards the vertical mixing in models as
 569 being the largest source of model error; too much or too little methane (or other trace gas) at the

570 surface as a result of incorrect mixing leads to inaccurate surface flux calculations (e.g. Jiang et
 571 al. 2013; Schuh et al. 2019; Mcnorton et al. 2020). These studies show that this effect is largest
 572 in the tropics where there is significant convection with an uncertainty that is about the same size
 573 as the data uncertainty. On the other hand, the mid-latitudes likely have smaller uncertainties of
 574 this type because of smaller uncertainties related to vertical mixing. For the purpose of this study
 575 we assume the model error is the same magnitude as the observation error \mathbf{S}_n ; however continued
 576 advances are needed in both quantifying and mitigating this term, and how it affects the
 577 emissions estimates, in order to improve confidence in the comparisons between inventories and
 578 satellite data.

579 Note that if the GOSAT-based emissions are directly compared to the inventory without
 580 first passing the inventory through the inversion operator, then the uncertainties in the
 581 comparison are much larger and less meaningful as they include both the smoothing error of the
 582 data and the full uncertainty of the inventory:

$$583$$

$$584 E\|\hat{\mathbf{z}} - \mathbf{z}_i\| = \mathbf{S}_i + \mathbf{S}_n + \mathbf{S}_m + (\mathbf{I}-\mathbf{A})\mathbf{S}_A(\mathbf{I}-\mathbf{A})^T \quad (16)$$

$$585$$

$$586$$

587 As a demonstration, we compare the GOSAT based emissions to the inventories both directly
 588 (uncertainties from Equation 16) and after applying the inversion operator (e.g. see Figures 2-4).

589

590 **Use of Prior Swapping to evaluate emissions:** Equation 3 represents an alternative but
 591 equivalent approach for mitigating smoothing error when comparing atmospheric based
 592 emissions estimates to an inventory. After “swapping” the prior used for the GOSAT based
 593 emissions estimate with the inventory the new estimate has the following form:

$$594$$

$$595 \hat{\mathbf{z}}_{\text{GOSAT_New}} = \mathbf{z}_I + \mathbf{A}(\mathbf{z}_{\text{True}} - \mathbf{z}_I) + \boldsymbol{\delta}_n + \boldsymbol{\delta}_m \quad (17)$$

$$596$$

597 In this instance we want to take the expectation of the difference of $\hat{\mathbf{z}}_{\text{GOSAT_New}}$ and \mathbf{z}_I as
 598 Equation (3) is equivalent to using \mathbf{z}_I as the *a priori* in the inversion described by Equation 1:

$$599$$

$$600 \hat{\mathbf{z}}_{\text{GOSAT_New}} - \mathbf{z}_I = \mathbf{A}(\mathbf{z}_{\text{True}} - \mathbf{z}_I) = \mathbf{A}(\boldsymbol{\delta}_I) + \boldsymbol{\delta}_n + \boldsymbol{\delta}_m \quad (18)$$

601
602 Equation 18 is the same as Equation 14 which demonstrates that the covariances as described by
603 Equation 15 (and hence uncertainties) are the same using prior swapping or an inversion operator
604 approach.

605

606

607 **Appendix C: Description of Inventories**

608

609

610 **(EPA GHGI)** The U.S. Environmental Protection Agency's (EPA) Inventory of U.S.
611 Greenhouse Gas Emissions and Sinks (GHGI) provides annual estimates of methane emissions
612 from anthropogenic sources. The gridded inventory used here covers emissions from sectors
613 such as agriculture, energy, waste, and coal for the years 2012 to 2018 (Maasakkers et al. 2023).
614 Desai et al. (2026) provides updated national-scale inventory estimates for 1990–2024 that are
615 methodologically consistent with the EPA GHGI, allowing a comparable gridded product to be
616 developed and evaluated against satellite-based inversions using the benchmark framework
617 applied here.

618 1. **Total Methane Emissions:** Gridded GHGI reports U.S. CONUS methane
619 emissions in 2015 at **23.7 Tg** of CH₄, which accounts for approximately **7% of global**
620 **anthropogenic methane emissions.**

621 2. **Sectoral Breakdown:** The Gridded GHGI includes methane emissions of 26
622 individual sectors. The largest sources are (see Table 2):

- 623 ○ **Livestock and Rice:** Emissions from enteric fermentation and manure
624 management constitute a significant portion of methane emissions from this sector
625 (8.8), with total agricultural emissions reaching **9.4 Tg** in 2018.
- 626 ○ **Oil and Gas:** Methane emissions from the oil and gas sectors, including
627 production & exploration, refining, transmission & storage, processing, and
628 distribution, account for approximately **6.9 Tg**.

- 629 ○ **Waste:** Emissions from municipal solid waste (MSW) landfills, industrial
630 landfills, wastewater treatment, and composting contributed to about **4.8 Tg**.
- 631 ○ **Coal Mines:** Methane from coal mining, including both active and abandoned
632 mines, contributed approximately **2.5 Tg**.

633 3. **Methodology:** The GHGI combines activity data with emission factors to
634 estimate methane emissions. The inventory uses data from sources such as the EPA’s
635 Greenhouse Gas Reporting Program (GHGRP) and U.S. Department of Agriculture
636 (USDA). The gridded GHGI uses facility-level data as well as proxy data for sources
637 with limited spatial information. to spatially and temporally disaggregate emissions

638 4. **Uncertainty and Adjustments:** The uncertainty in methane emissions is
639 accounted for with confidence intervals provided in the GHGI report. Recent updates to
640 the GHGI methodology include the inclusion of large well blowouts and emissions from
641 abandoned oil and gas wells, which had not been considered in previous iterations. The
642 inventory is continuously updated to reduce uncertainties and improve accuracy.

643 5. **Comparisons with Atmospheric Data:** The Gridded GHGI serves as a critical
644 input for atmospheric inversions and can be compared with top-down estimates from
645 satellite-based data, such as those from GOSAT.

646 **(EDGAR 2024)** The Emissions Database for Global Atmospheric Research

647
648 The EDGAR series of inventories provides gridded (0.1x0.1 degree) emissions of the key
649 anthropogenic emissions contributing to the global methane budget. We refer the reader to
650 Crippa et al. (2020, 2024) for a description of this inventory. Emissions are generated by
651 downscaling national totals by sector using spatial proxies and projected to the 0.1 x 0.1 grid. In
652 order to improve the accuracy of comparisons between the EDGAR inventory and the GOSAT-
653 based fluxes, we regrid their sub-categories to livestock, waste, coal, gas, oil, and rice (e.g. see
654 Figure 1 for the EDGAR 2024 oil&gas emissions).

655

656 (NOAA FOG) The NOAA fuel-based oil and gas (FOG) inventory provides oil and gas
657 emissions for the contiguous United States (CONUS) gridded at 4km x 4km and are then
658 regridded to (0.1 x 0.1 degree) for this work (Francoeur et al. 2021). The NOAA FOG methane
659 emissions inventory is generated through a hybrid approach that combines activity data with
660 atmospheric measurements to provide a more comprehensive and accurate assessment of
661 methane emissions from the oil and gas sector. FOG combines combustion activity of drilling
662 and production engines with fuel-based nitrogen oxides (NO_x) emission factors from
663 measurements and empirical models (Gorchov-Negron *et al.* 2018). The activity-based NO_x
664 emissions have been evaluated with airborne NOAA WP-3 measurements over a comprehensive
665 number of US oil and gas basins during the Southeast Nexus Study
666 (<https://csl.noaa.gov/projects/senex/>) and Shale Oil and Natural Gas Nexus Study
667 (<https://csl.noaa.gov/projects/songnex/>), as well as with spaceborne observations (Dix *et al.*
668 2020, 2022). Oil and gas methane emissions are then inferred by tracer-tracer ratios observed by
669 the aircraft relative to NO_x analyzed for each oil and gas basin measured (Francoeur *et al.* 2021).
670 The hybrid approach in principle allows for a better representation of emissions compared to
671 traditional activity-based inventories as the atmospheric data likely better captures the effect of
672 **fugitive emissions** and other hard-to-measure sources that are often underrepresented in other
673 activity based inventory methods. Additionally, atmospheric measurements help to address
674 uncertainties by cross-referencing emission estimates with observed methane concentrations,
675 thus improving the overall reliability of the inventory.

676 Key findings from the FOG inventory include:

- 677 1. **Methane Emissions:** The FOG inventory estimates total methane emissions from
678 oil and natural gas production **at 14.1 ± 2.0 Tg CH₄/yr for 2015.**
- 679 2. **Sectoral Breakdown:** The FOG inventory includes methane emissions from
680 drilling, production, gathering, and processing activities. The contribution of methane
681 emissions from the production and drilling phases is particularly significant, comprising
682 about **60% of total methane emissions** during the oil and gas production process.
- 683 3. **Uncertainty and Evaluation:** The methane estimates from the FOG inventory
684 are supported by aircraft-derived "top-down" emission measurements, which help

685 validate the inventory's accuracy. Uncertainties are evaluated through a Monte-Carlo
686 analysis of the NO_x emissions and emissions factors (Francoeur *et al.* 2021)

687

688 **Code Availability**

689 The code for the sectoral attribution is available here (Worden and Pandey 2025):

690 <https://doi.org/10.5281/zenodo.15786798>].

691 A Python notebook demonstrating the benchmarking approach with the GOSAT inversion fluxes
692 is available at Pandey, S., & Worden, J. (2025). Evaluation of Methane Emissions Inventory
693 Using Satellite Flux Inversions Data set <https://doi.org/10.5281/zenodo.16921536> (Pandey and
694 Worden 2025)

695

696 **Data Availability**

697 GOSAT-based fluxes and emissions by sector are also available on Zenodo:

698 <https://zenodo.org/records/15786798>. (Worden and Pandey 2025)

699

700 **Author Contributions**

701 JW designed the study, performed sectoral attribution, and wrote the paper draft SP performed
702 the inventory comparison analysis, made the figures and supported the paper writing. HN, JDM,
703 and KB supported the analysis and paper writing. CH and CL supported the FOG analysis. DG
704 and LS supported interpretation of the inventories. DJ, LE, DV, JE, and ZQ produced the
705 GOSAT fluxes, supported the interpretation, and reviewed the paper.

706

707 **Competing Interests: The authors declare that to their knowledge there are no competing**
708 **interests.**

709

710 **Acknowledgements**

711

712 Part of this research was carried out at the Jet Propulsion Laboratory, California Institute of
713 Technology, under a contract with the National Aeronautics and Space Administration. Chatgpt
714 used to support paper editing.

715

716 **Financial Support**

717

718 This work is funded by the NASA Carbon Monitoring System (Carbon Monitoring System
719 NNH23ZDA001N-CMS) and through the NASA Greenhouse Gas Center.

720 **References**

721

722 Alvarez, R. A., Zavala-Araiza, D., Lyon, D. R., Allen, D. T., Barkley, Z. R., Brandt, A. R., et al.
723 (2018). Assessment of methane emissions from the U.S. oil and gas supply chain. *Science*,
724 361(6398), eaar7204. <https://doi.org/10.1126/science.aar7204>

725 Barkley, Z. R., Lauvaux, T., Davis, K. J., Miles, N. L., Richardson, S. J., Jacobson, G., et al.
726 (2022). Estimating methane emissions from the Marcellus and Delaware Basins using continuous
727 tower observations. *Atmospheric Chemistry and Physics*, 23, 6127–6145.
728 <https://doi.org/10.5194/acp-23-6127-2023>

729 Bowman, K. W., Rodgers, C. D., Kulawik, S. S., Worden, J., Sarkissian, E., Osterman, G., Steck,
730 T., Lou, M., Eldering, A., Shephard, M., Worden, H., Lampel, M., Clough, S., Brown, P.,
731 Rinsland, C., Gunson, M., and Beer, R.: Tropospheric Emission Spectrometer: Retrieval Method
732 and Error Analysis, *Ieee T Geosci Remote*, 44, 1297–1307,
733 <https://doi.org/10.1109/tgrs.2006.871234>, 2006.

734 Crippa, M., Solazzo, E., Huang, G., Guizzardi, D., Koffi, E., Muntean, M., et al. (2020). High
735 resolution temporal profiles in the Emissions Database for Global Atmospheric Research.
736 *Scientific Data*, 7, 121. <https://doi.org/10.1038/s41597-020-0462-2>

737 Crippa, M., Guizzardi, D., Pagani, F., Schiavina, M., Melchiorri, M., Pisoni, E., et al. (2024).
738 Insights into the spatial distribution of global, national, and subnational greenhouse gas
739 emissions in the Emissions Database for Global Atmospheric Research (EDGAR v8.0). *Earth*
740 *System Science Data*, 16(6), 2811–2830. <https://doi.org/10.5194/essd-16-2811-2024>

741 Crippa, M., Guizzardi, D., Pagani, F., Banja, M., Muntean, M., Schaaf, E., Monforti-Ferrario, F.,
742 Becker, W., Quadrelli, R., Risquez Martin, A., Taghavi-Moharamli, P., Köykkä, J., Grassi, G.,
743 Rossi, S., Melo, J., Oom, D., Branco, A., San-Miguel, J., Manca, G., Pisoni, E., Vignati, E. and
744 Pekar, F., GHG emissions of all world countries, Publications Office of the European Union,
745 Luxembourg, 2024, doi:10.2760/4002897, JRC138862

746

747 Cusworth, D. H., Bloom, A. A., Ma, S., Miller, C. E., Bowman, K., Yin, Y., et al. (2021). A
748 Bayesian framework for deriving sector-based methane emissions from top-down fluxes.
749 *Communications Earth & Environment*, 2, 242. <https://doi.org/10.1038/s43247-021-00312-6>

750 Cusworth, D. H., Duren, R. M., Ayasse, A. K., Jiorle, R., Howell, K., Aubrey, A., et al. (2024).
751 Quantifying methane emissions from United States landfills. *Science*, 383(6690), 1499–1504.
752 <https://doi.org/10.1126/science.adi7735>

753 Cusworth, D. H., Duren, R. M., Thorpe, A. K., Tseng, E., Thompson, D., Guha, A., et al. (2020).
754 Using remote sensing to detect, validate, and quantify methane emissions from California solid
755 waste operations. *Environmental Research Letters*, 15, 054012. [https://doi.org/10.1088/1748-](https://doi.org/10.1088/1748-9326/ab7b99)
756 [9326/ab7b99](https://doi.org/10.1088/1748-9326/ab7b99)

757 Cusworth, D. H., Thorpe, A. K., Ayasse, A. K., Stepp, D., Heckler, J., Asner, G. P., et al. (2022).
758 Strong methane point sources contribute a disproportionate fraction of total emissions across
759 multiple basins in the United States. *Proceedings of the National Academy of Sciences*, 119,
760 e2202338119. <https://doi.org/10.1073/pnas.2202338119>

761 Desai, M., Camobreco, V., Hedger, T., Irving, W., Rewcastle, K., Steller, J., Barbieri,
762 L., Weitz, M., Murumkar, T., Fawcett, A., Lou, J., Cui, R., and Hultman, N.: *Greenhouse*
763 *Gas Inventory and Analysis for the United States: 1990–2024*, Center for Global
764 Sustainability, University of Maryland, College Park, 2026.

765 Dix, B., Francoeur, C., Li, M., Serrano-Calvo, R., Levelt, P. F., Veefkind, J. P., McDonald, B.
766 C., and de Gouw, J. A.: Quantifying NO_x emissions from U.S. oil and gas production regions
767 using TROPOMI NO₂, *ACS Earth Space Chem.*, **6**(2), 403-414,
768 <https://doi.org/10.1021/acsearthspacechem.1c00387>, 2022.
769

770 Dix, B., Bruin, J., Roosenbrand, E., Vlemmix, T., Francoeur, C., Gorchov-Negron, A. M.,
771 McDonald, B., Zhizhin, M., Elvidge, C., Veefkind, P., Levelt, P., and de Gouw, J. A.: Nitrogen
772 oxide emissions from U.S. oil and gas production: Recent trends and source
773 attribution, *Geophys. Res. Lett.*, **47**(1), e2019GL085866, <https://doi.org/10.1029/2019GL085866>,
774 2020.
775

776 East, J. D., Jacob, D. J., Jarvis, D., Balasus, N., Estrada, L. A., Hancock, S. E., Sulprizio, M. P.,
777 Thomas, J., Wang, X., Chen, Z., Varon, D. J., and Worden, J. R.: Worldwide inference of
778 national methane emissions by inversion of satellite observations with UNFCCC prior estimates,
779 *Nat. Commun.*, **16**, 11004, <https://doi.org/10.1038/s41467-025-67122-8>, 2025.

780 [EDGAR \(Emissions Database for Global Atmospheric Research\) Community GHG Database, a](#)
781 [collaboration between the European Commission, Joint Research Centre \(JRC\), the International](#)
782 [Energy Agency \(IEA\), and comprising IEA-EDGAR CO₂, EDGAR CH₄, EDGAR N₂O,](#)
783 [EDGAR F-GASES version 2024 European Commission, JRC \(Datasets\).](#)
784 https://edgar.jrc.ec.europa.eu/dataset_ghg2024 (accessed: 1 October 2025)

785

786 [EPA \(U.S. Environmental Protection Agency\). \(2011\). Fact Sheet on Mandatory Reporting of](#)
787 [Greenhouse Gases \(40 CFR part 98\). \[https://www.epa.gov/sites/default/files/2015-\]\(https://www.epa.gov/sites/default/files/2015-07/documents/part98factsheet.pdf\)](#)
788 [07/documents/part98factsheet.pdf](#)

789 Etiope, G., Ciotoli, G., Schwietzke, S., & Schoell, M. (2018). Gridded maps of geological
790 methane emissions and their isotopic signature. *Earth System Science Data*, **11**, 1–22.
791 <https://doi.org/10.5194/essd-11-1-2019>

792 Francoeur, C. B., McDonald, B. C., Gilman, J. B., Zarzana, K. J., Dix, B., Brown, S. S., et al.
793 (2021). Quantifying methane and ozone precursor emissions from oil and gas production regions
794 across the contiguous US. *Environmental Science & Technology*, 55(13), 9129–9139.
795 <https://doi.org/10.1021/acs.est.0c07352>

796 Gorchov Negron, A. M., McDonald, B. C., McKeen, S. A., Peischl, J., Ahmadov, R., de Gouw,
797 J. A., Frost, G. J., Hastings, M. G., Pollack, I. B., Ryerson, T. B., Thompson, C., Warneke, C.,
798 and Trainer, M.: Development of a fuel-based oil and gas inventory of nitrogen oxides
799 emissions, *Environ. Sci. Technol.*, **52**, 10175–10185, <https://doi.org/10.1021/acs.est.8b02245>,
800 2018.

801 [Gordon, D. No Standard Oil: Managing Abundant Petroleum in a Warming World \(paperback
802 edition\). Oxford University Press, 2025. https://global.oup.com/academic/product/no-standard-
803 oil-9780197832165?cc=us&lang=en&](https://global.oup.com/academic/product/no-standard-oil-9780197832165?cc=us&lang=en&)

804 Hancock, S. E., Jacob, D., Chen, Z., Nesser, H., Davitt, A., Varon, D. J., et al. (2025). Satellite
805 quantification of methane emissions from South American countries: A high-resolution inversion
806 of TROPOMI and GOSAT observations. *Atmospheric Chemistry and Physics*, 25, 797–833.
807 <https://doi.org/10.5194/acp-25-797-2025>

808 Herman, R. L., Cherry, J. E., Young, J., Welker, J. M., Noone, D., Kulawik, S. S., & Worden, J.
809 (2014). Aircraft validation of Aura Tropospheric Emission Spectrometer retrievals of HDO /
810 H₂O. *Atmospheric Measurement Techniques*, 120(9), 3127–3138. [https://doi.org/10.5194/amt-7-
811 3127-2014](https://doi.org/10.5194/amt-7-3127-2014)

812

813 Hmiel, B., Petrenko, V. V., Dyonisius, M. N., Buizert, C., Smith, A. M., Place, P. F., et al.
814 (2020). Preindustrial 14CH₄ indicates greater anthropogenic fossil CH₄ emissions. *Nature*, 578,
815 409–412. <https://doi.org/10.1038/s41586-020-1991-8>

816 Hristov, A. N., Harper, M., Meinen, R., Day, R., Lopes, J., Ott, T., et al. (2017). Discrepancies
817 and uncertainties in bottom-up gridded inventories of livestock methane emissions for the
818 contiguous United States. *Environmental Science & Technology*, 51(23), 13668–13677.
819 <https://doi.org/10.1021/acs.est.7b03332>

820 [IEA \(International Energy Agency\). \(2025\). Global Methane Tracker 2025.](#)
821 <https://www.iea.org/reports/global-methane-tracker-2025/key-findings>

822 Jacob, D. J., Varon, D. J., Cusworth, D. H., Dennison, P. E., Frankenberg, C., Gautam, R., et al.
823 (2022). Quantifying methane emissions from the global scale down to point sources using
824 satellite observations of atmospheric methane. *Atmospheric Chemistry and Physics*, 22, 9617–
825 9646. <https://doi.org/10.5194/acp-22-9617-2022>

826 Janardanan, R., Maksyutov, S., Wang, F., Nayagam, L., Sahu, S. K., Mangaraj, P., et al. (2024).
827 Country-level methane emissions and their sectoral trends during 2009–2020 estimated by high-
828 resolution inversion of GOSAT and surface observations. *Environmental Research Letters*, 19,
829 034007. <https://doi.org/10.1088/1748-9326/ad2436>

830 Kruskamp, N., Lohman, H., Burnette, A., Coxen, C., Ellermeier, N., Bollenbacher, J., Powers, J.,
831 Coffield, S., Farhat, Y., and Maasakkers, J.: *Gridded U.S. Anthropogenic Methane Greenhouse*
832 *Gas Inventory (gridded GHGI)*, Zenodo, <https://doi.org/10.5281/zenodo.16782735>, 2025.

833 Kort, E. A., Eluszkiewicz, J., Stephens, B. B., Miller, J. B., Gerbig, C., Nehrkorn, T., et al.
834 (2008). Emissions of CH₄ and N₂O over the United States and Canada based on a receptor-
835 oriented modeling framework and COBRA-NA atmospheric observations. *Geophysical*
836 *Research Letters*, 35, L18808. <https://doi.org/10.1029/2008GL034031>

837 Lu, X., Jacob, D. J., Zhang, Y., Shen, L., Sulprizio, M. P., Maasakkers, J. D., et al. (2023).
838 Observation-derived 2010–2019 trends in methane emissions and intensities from U.S. oil and
839 gas fields tied to activity metrics. *Proceedings of the National Academy of Sciences*, 120,
840 e2217900120. <https://doi.org/10.1073/pnas.2217900120>

841 Maasakkers, J. D., Jacob, D. J., Sulprizio, M. P., Scarpelli, T. R., Nesser, H., Sheng, J., et al.
842 (2021). 2010–2015 North American methane emissions, sectoral contributions, and trends: a
843 high-resolution inversion of GOSAT observations of atmospheric methane. *Atmospheric*
844 *Chemistry and Physics*, 21, 4339–4356. <https://doi.org/10.5194/acp-21-4339-2021>

845 Maasakkers, J. D., McDuffie, E. E., Sulprizio, M. P., Chen, C., Schultz, M., Brunelle, L., et al.
846 (2023). A gridded inventory of annual 2012–2018 U.S. anthropogenic methane emissions.

847 *Environmental Science & Technology*, 57(43), 16276–16288.
848 <https://doi.org/10.1021/acs.est.3c05138>

849 Miller, S. M., Wofsy, S. C., Michalak, A. M., Kort, E. A., Andrews, A. E., Biraud, S. C., et al.
850 (2013). Anthropogenic emissions of methane in the United States. *Proceedings of the National*
851 *Academy of Sciences*, 110(50), 20018–20022. <https://doi.org/10.1073/pnas.1314392110>

852 Nesser, H., Jacob, D. J., Maasackers, J. D., Lorente, A., Chen, Z., Lu, X., et al. (2024). High-
853 resolution U.S. methane emissions inferred from an inversion of 2019 TROPOMI satellite data:
854 Contributions from individual states, urban areas, and landfills. *Atmospheric Chemistry and*
855 *Physics*, 24, 5069–5091. <https://doi.org/10.5194/acp-24-5069-2024>

856 Nisbet, E. G., Manning, M. R., Dlugokencky, E. J., Fisher, R. E., Lowry, D., Michel, S. E., et al.
857 (2019). Very strong atmospheric methane growth in the 4 years 2014–2017: Implications for the
858 Paris Agreement. *Global Biogeochemical Cycles*, 33, 318–342.
859 <https://doi.org/10.1029/2018GB006009>

860 Pandey, S., Worden, J., Cusworth, D. H., Varon, D. J., Thill, M. D., Jacob, D. J., and Bowman,
861 K. W.: Relating multi-scale plume detection and area estimates of methane emissions: a
862 theoretical and empirical analysis, *Environ. Sci. Technol.*, 59, 7931–7947,
863 <https://doi.org/10.1021/acs.est.4c07415>, 2025.

864 Pandey, S. and Worden, J.: *Evaluation of Methane Emissions Inventory Using Satellite Flux*
865 *Inversions* (data set), Zenodo, <https://doi.org/10.5281/zenodo.16921536>, 2025.

866 Parker, R., Boesch, H., Cogan, A., Fraser, A., Feng, L., Palmer, P. I., et al. (2011). Methane
867 observations from the Greenhouse Gases Observing SATellite: Comparison to ground-based
868 TCCON data and model calculations. *Geophysical Research Letters*, 38, L15807.
869 <https://doi.org/10.1029/2011GL047871>

870 Petrescu, A. M. R., Peters, G. P., Engelen, R., Houweling, S., Brunner, D., Tsuruta, A., et al.
871 (2024). Comparison of observation- and inventory-based methane emissions for eight large
872 global emitters. *Earth System Science Data*, 16, 4325–4350. [https://doi.org/10.5194/essd-16-](https://doi.org/10.5194/essd-16-4325-2024)
873 [4325-2024](https://doi.org/10.5194/essd-16-4325-2024)

874 Qu, Z., Jacob, D. J., Zhang, Y., Shen, L., Varon, D. J., Lu, X., Scarpelli, T., Bloom, A., Worden,
875 J., and Parker, R. J.: Attribution of the 2020 surge in atmospheric methane by inverse analysis of
876 GOSAT observations, *Environ Res Lett*, <https://doi.org/10.1088/1748-9326/ac8754>, 2022.

877 Qu, Z., Jacob, D. J., Bloom, A. A., Worden, J. R., Parker, R. J., & Boesch, H. (2024). Inverse
878 modeling of 2010–2022 satellite observations shows that inundation of the wet tropics drove the
879 2020–2022 methane surge. *Proceedings of the National Academy of Sciences*, 121,
880 e2402730121. <https://doi.org/10.1073/pnas.2402730121>

881 Rodgers, C. D., & Connor, B. J. (2003). Intercomparison of remote sounding instruments.
882 *Journal of Geophysical Research: Atmospheres*, 108, 4116.
883 <https://doi.org/10.1029/2002JD002299>

884 Saunio, M., Stavert, A. R., Poulter, B., Bousquet, P., Canadell, J. G., Jackson, R. B., et al.
885 (2020). The global methane budget 2000–2017. *Earth System Science Data*, 12, 1561–1623.
886 <https://doi.org/10.5194/essd-12-1561-2020>

887 Sherwin, E. D., Rutherford, J. S., Zhang, Z., Chen, Y., Wetherley, E. B., Yakovlev, P. V., et al.
888 (2024). U.S. oil and gas system emissions from nearly one million aerial site measurements.
889 *Nature*, 627, 328–334. <https://doi.org/10.1038/s41586-024-07117-5>

890 United States Environmental Protection Agency (EPA). (2023). Inventory of U.S. greenhouse
891 gas emissions and sinks: 1990–2021 (EPA 430-R-23-002). Retrieved from
892 <https://www.epa.gov/ghgemissions/inventory-us-greenhouse-gas-emissions-and-sinks>

893 Wecht, K. J., Jacob, D. J., & Sulprizio, M. P. (2014). Spatially resolving methane emissions in
894 California: constraints from the CalNex aircraft campaign and from present (GOSAT, TES) and
895 future (TROPOMI, *Atmospheric Chemistry and Physics*, 14(15). [https://doi.org/10.5194/acp-](https://doi.org/10.5194/acp-14-8173-2014)
896 14-8173-2014

897

898 Wolf, J., Asrar, G. R., & West, T. O. (2017). Revised methane emissions factors and spatially
899 distributed annual carbon fluxes for global livestock. *Carbon Balance and Management*, 12, 16.
900 <https://doi.org/10.1186/s13021-017-0084-y>

901 Worden, J., Kulawik, S., Shepard, M., Clough, S., Worden, H., Bowman, K., and Goldman, A.:
902 Predicted errors of tropospheric emission spectrometer nadir retrievals from spectral window
903 selection, *J Geophys Res Atmospheres* 1984 2012, 109, D09308,
904 <https://doi.org/10.1029/2004jd004522>, 2004.
905

906 Worden, J. R., Cusworth, D. H., Qu, Z., Yin, Y., Zhang, Y., Bloom, A. A., et al. (2022). The
907 2019 methane budget and uncertainties at 1° resolution and each country through Bayesian
908 integration of GOSAT total column methane data and a priori inventory estimates. *Atmospheric*
909 *Chemistry and Physics*, 22, 6811–6841. <https://doi.org/10.5194/acp-22-6811-2022>

910 Worden, J. R., Pandey, S., Zhang, Y., Cusworth, D. H., Qu, Z., Bloom, A. A., et al. (2023).
911 Verifying methane inventories and trends with atmospheric methane data. *AGU Advances*, 4.
912 <https://doi.org/10.1029/2023AV000871>

913 Worden, J. R. and Pandey, S.: *Evaluation of Methane Emissions Inventory Using Satellite Flux*
914 *Inversions*, Zenodo, <https://doi.org/10.5281/zenodo.15786798>, 2025.

915 [World Bank. \(2025\). Global Gas Flaring Tracker Report.](https://thedocs.worldbank.org/en/doc/bd2432bbb0e514986f382f61b14b2608-0400072025/original/Global-Gas-Flaring-Tracker-Report-July-2025.pdf)
916 [https://thedocs.worldbank.org/en/doc/bd2432bbb0e514986f382f61b14b2608-](https://thedocs.worldbank.org/en/doc/bd2432bbb0e514986f382f61b14b2608-0400072025/original/Global-Gas-Flaring-Tracker-Report-July-2025.pdf)
917 [0400072025/original/Global-Gas-Flaring-Tracker-Report-July-2025.pdf](https://thedocs.worldbank.org/en/doc/bd2432bbb0e514986f382f61b14b2608-0400072025/original/Global-Gas-Flaring-Tracker-Report-July-2025.pdf)

918 Zavala-Araiza, D., Lyon, D. R., Alvarez, R. A., Davis, K. J., Harriss, R., Herndon, S. C., et al.
919 (2015). Reconciling divergent estimates of oil and gas methane emissions. *Proceedings of the*
920 *National Academy of Sciences*, 112, 15597–15602. <https://doi.org/10.1073/pnas.1522126112>

921 Zhang, Y., Jacob, D. J., Lu, X., Maasackers, J. D., Scarpelli, T. R., Sheng, J.-X., et al. (2021).
922 Attribution of the accelerating increase in atmospheric methane during 2010–2018 by inverse
923 analysis of GOSAT observations. *Atmospheric Chemistry and Physics*, 21, 3643–3666.
924 <https://doi.org/10.5194/acp-21-3643-2021>

925 Zhang, P., Zhang, Y., and Liang, R.: 2025: Correction of simulation biases in stratospheric
926 methane concentrations for the inverse analysis of satellite column observations, *J. Geophys.*
927 *Res.-Atmos.*, 30, <https://doi.org/10.1029/2024JD042596>.

928

929

930 [Figure Captions](#)

931

932 Figure 1: (Top Panels) Mean Emissions for Oil and Gas for 2015 (at 1x1 degree lon/lat gridding)
933 as calculated from the EPA, FOG, EDGAR inventories. (Bottom Panels) Differences between
934 FOG and EPA and EDGAR and EPA.

935

936 Figure 2: Comparison of the U.S. oil and gas (O&G) methane emissions in 2015 from the
937 GOSAT inversion with those from the FOG inventory. The upper left panel (a) shows the
938 GOSAT based estimate. The upper right panel (b) shows the original FOG emissions. The
939 middle left panel (c) shows the difference between the top two. The middle right panel shows the
940 difference between FOG emissions and GOSAT based emissions after applying the inversion
941 operator (denoted AK). All figures use 1x1 degree gridding; only differences larger than the
942 corresponding calculated uncertainty are shown. The bottom right panel (E) shows the diagonal
943 of the averaging kernel (or DOFS) corresponding to that location for oil and gas emissions.

944

945 Figure 3: Same as in Figure 2 but for the EDGAR inventory.

946

947 Figure 4: Same as in Figure 3 but for the EPA GHGI inventory.

948

949 **Figure 5:** Comparison of the integrated total oil and gas (O&G) emissions derived from GOSAT
950 with those from the FOG, EPA GHGI , and EDGAR 2024 inventories, both with and without the
951 inversion operator (AK) applied. Comparisons should be made between the GOSAT estimate
952 and the inventories with inversion operator (AK) applied.

953

954 **Figure 6:** Integrated totals for oil and gas emissions between 2012 and 2020. The GOSAT
955 inversion operator has been applied to the FOG, EPA GHGI , and EDGAR 2024 inventories; the
956 biases between the comparisons are therefore not due to the prior used with the GOSAT
957 inversion.

958 **Figure 7:** Similar to Figure 2 but for EDGAR 2024 livestock emissions

959

960 **Figure 8:** Similar to Figure 7 but for EPA GHGI livestock emissions

961

962 **Figure 9:** Comparison of the integrated livestock emissions derived from GOSAT with those
963 from the EPA GHGI and EDGAR 2024 inventories, both with and without the inversion
964 operator (AK) applied. Comparisons should be made between the GOSAT estimate and the
965 inventories with inversion operator (AK) applied.

966

967 **Figure 10:** Integrated totals for Livestock Emissions between 2012 and 2020. The inversion
968 operator has been applied to the inventories.

969

970 **Figure 11:** Similar to Figure 2 but for EDGAR 2024 waste emissions

971

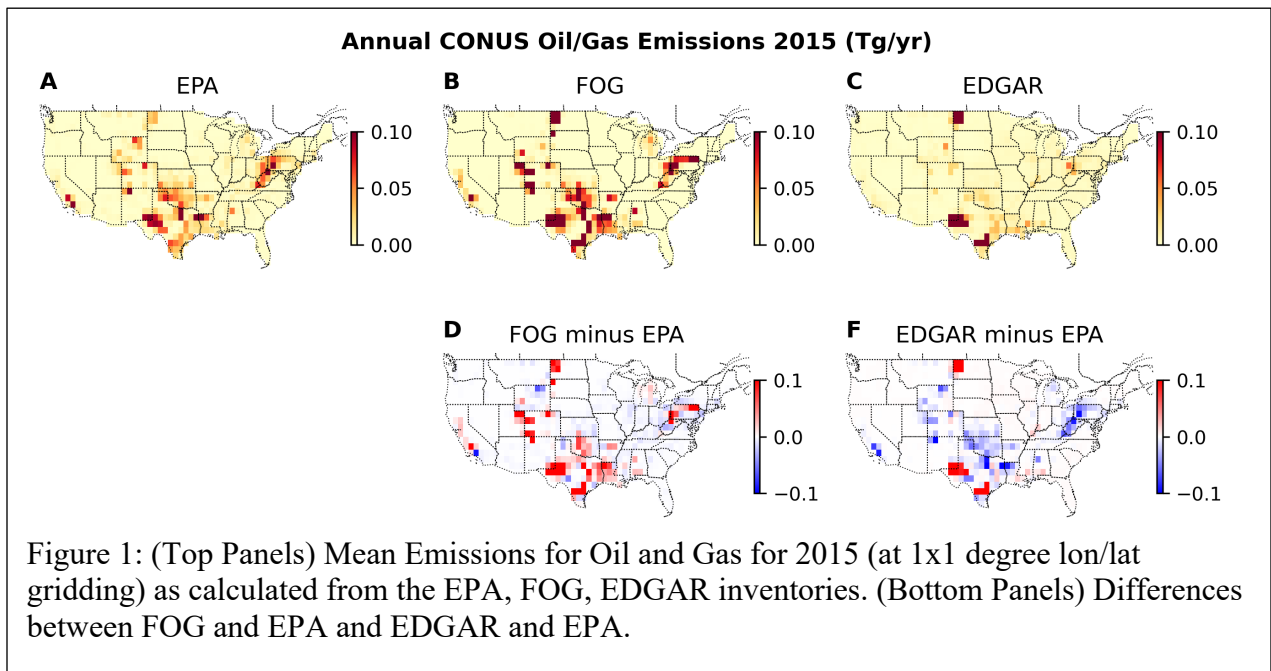
972 **Figure 12:** Similar to Figure 3 but for EPA GHGI waste emissions

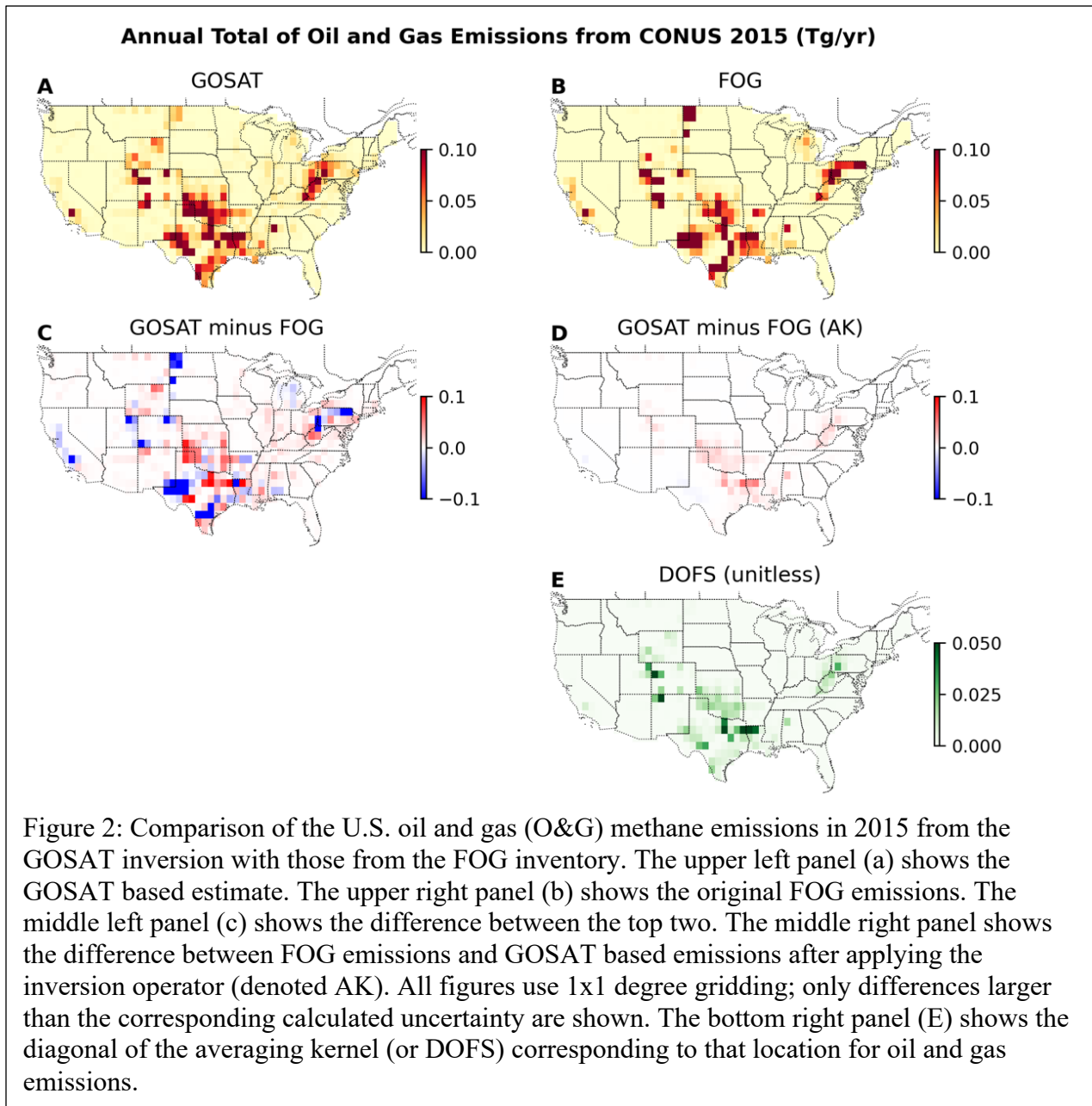
973

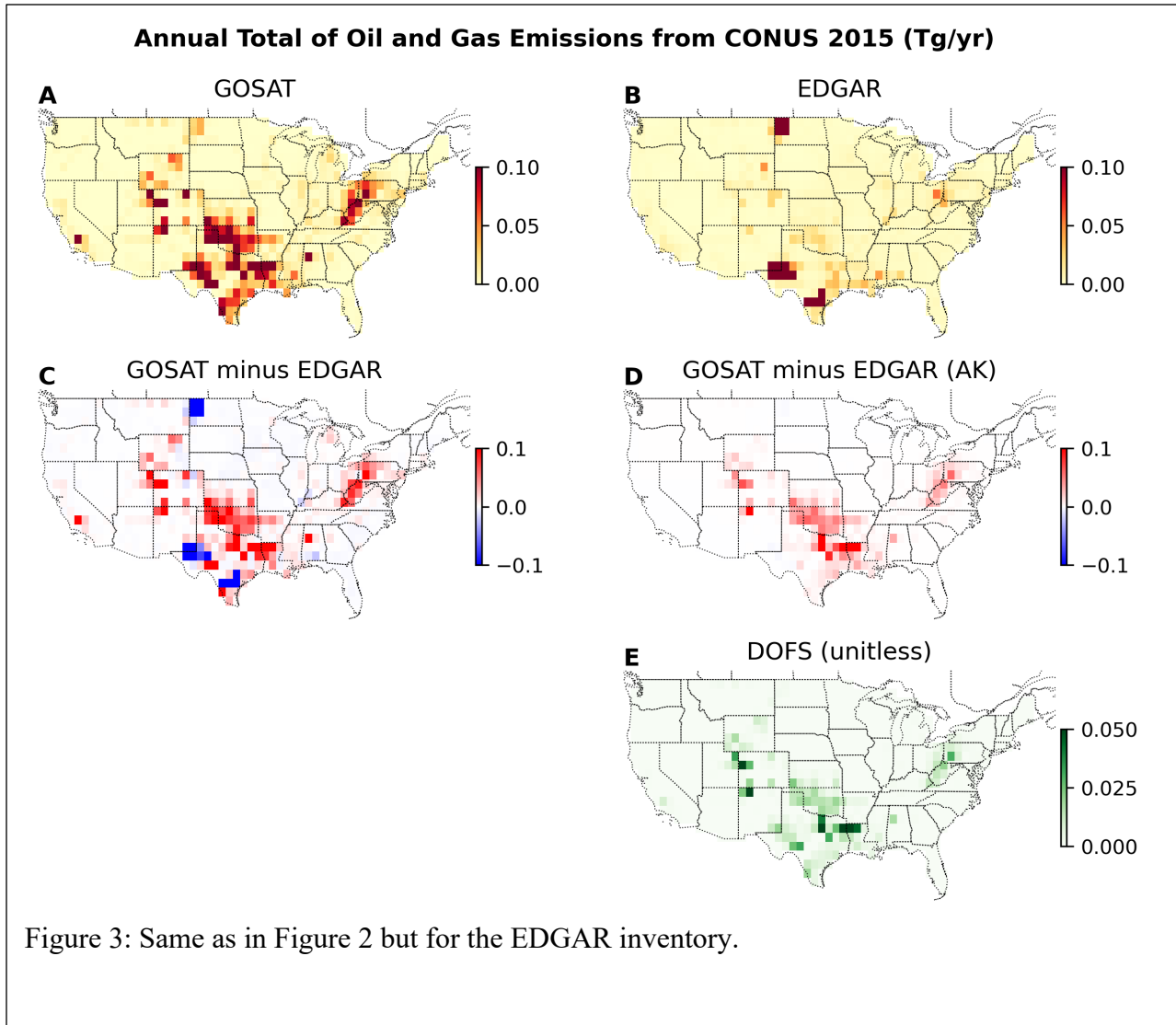
974 **Figure 13:** Integrated total methane emissions from the waste sector based on GOSAT, along
975 with estimates from the EPA GHGI and EDGAR 2024 inventories, both with and without the
976 inversion operator applied.

977

979







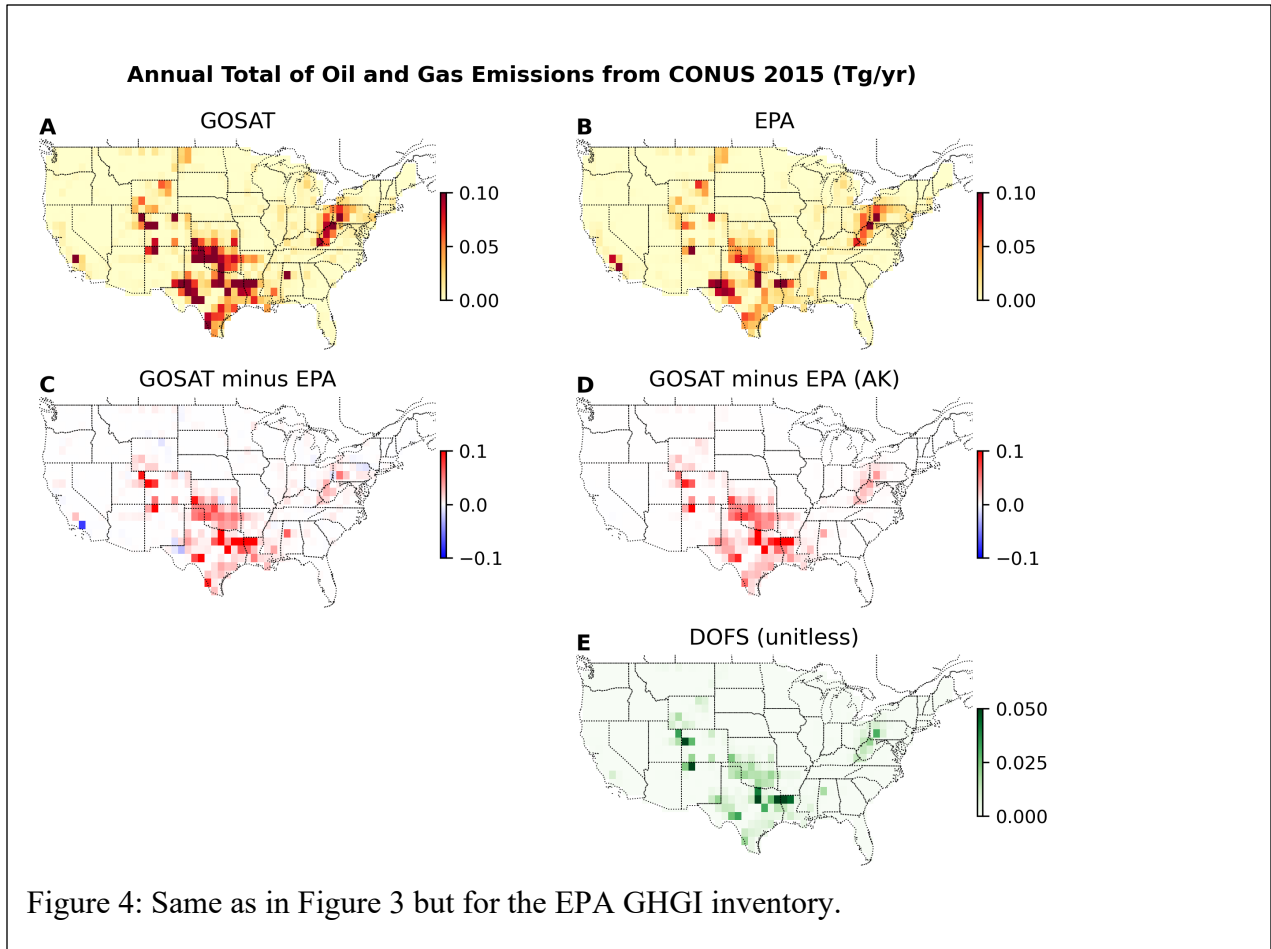
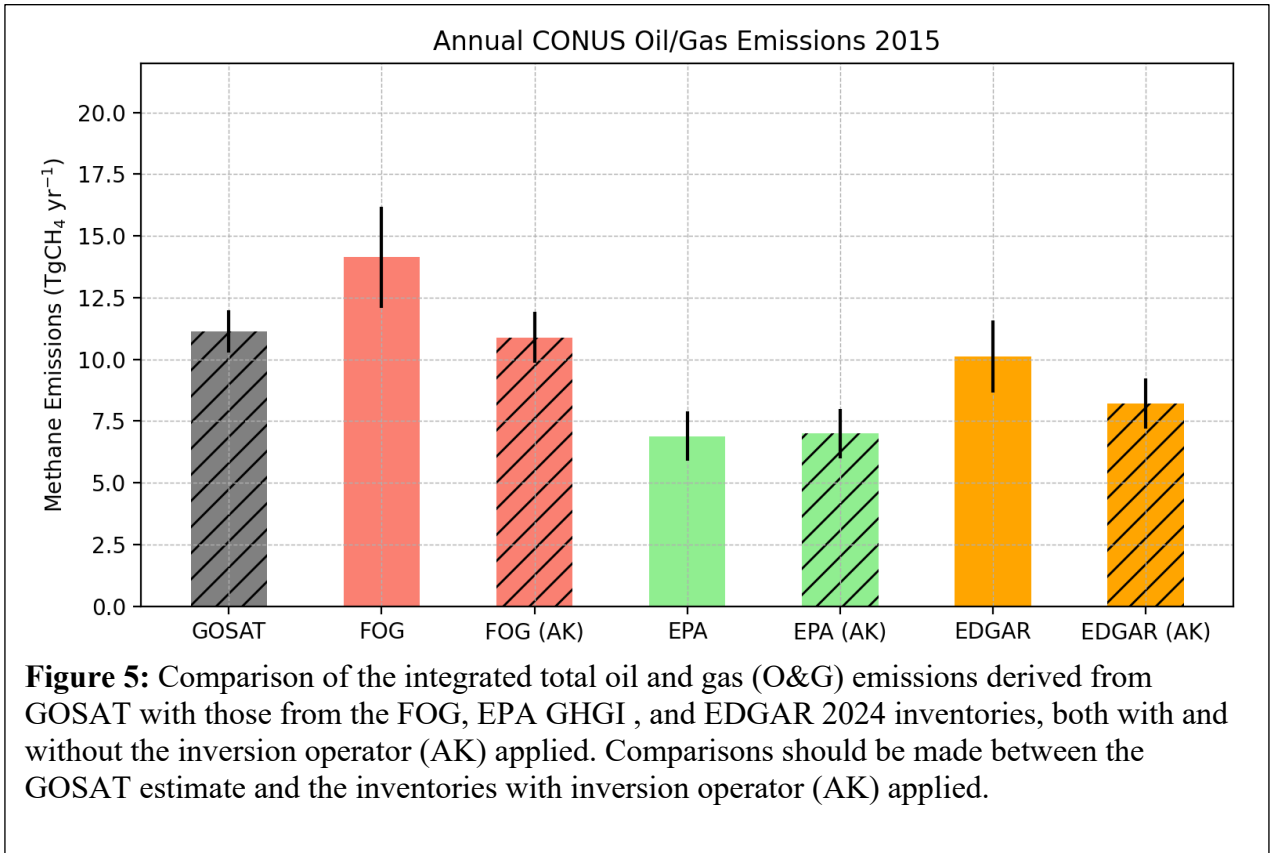
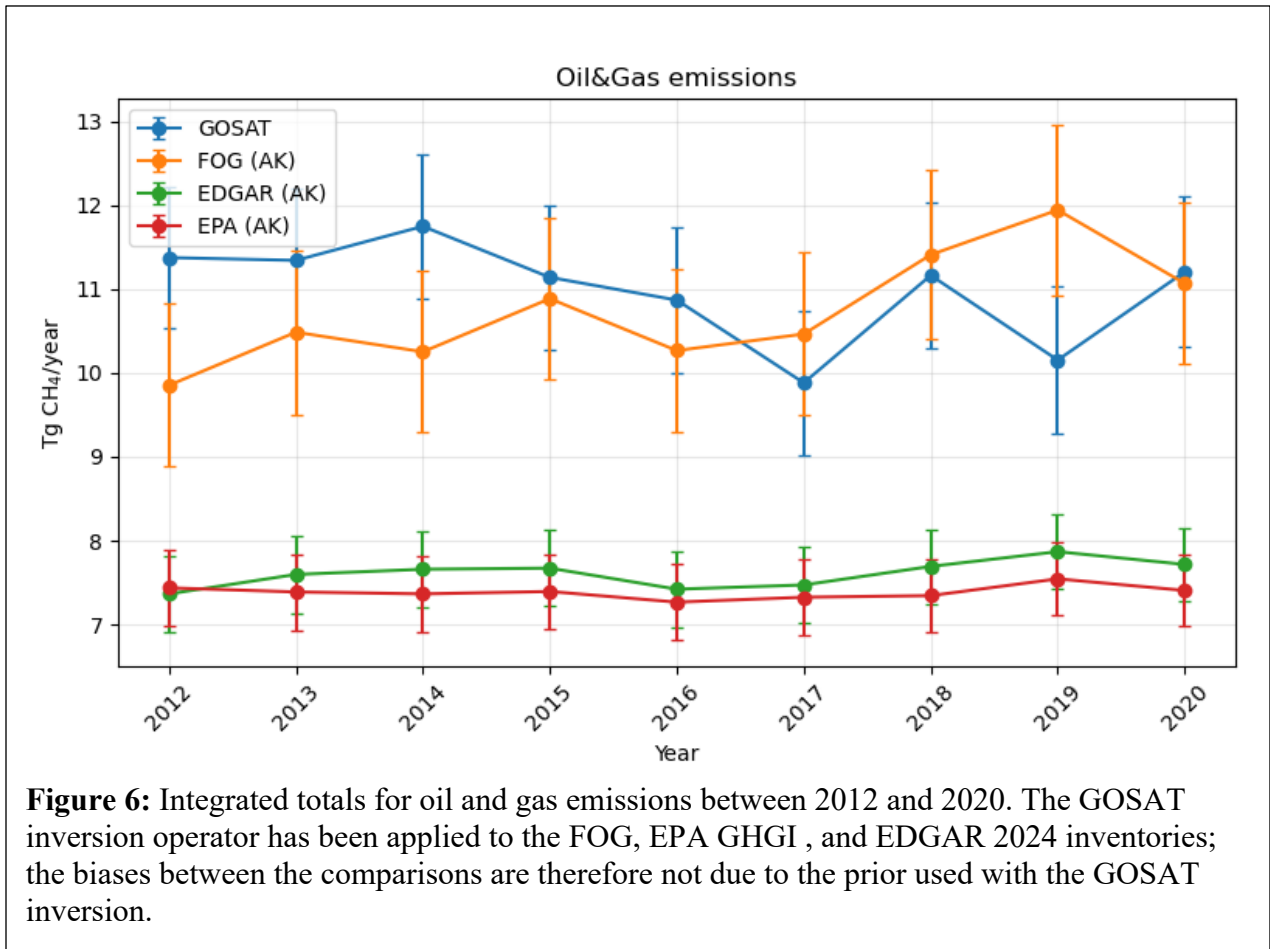


Figure 4: Same as in Figure 3 but for the EPA GHGI inventory.

983
984
985
986



987
988
989



990
991
992
993

Figure 6: Integrated totals for oil and gas emissions between 2012 and 2020. The GOSAT inversion operator has been applied to the FOG, EPA GHGI, and EDGAR 2024 inventories; the biases between the comparisons are therefore not due to the prior used with the GOSAT inversion.

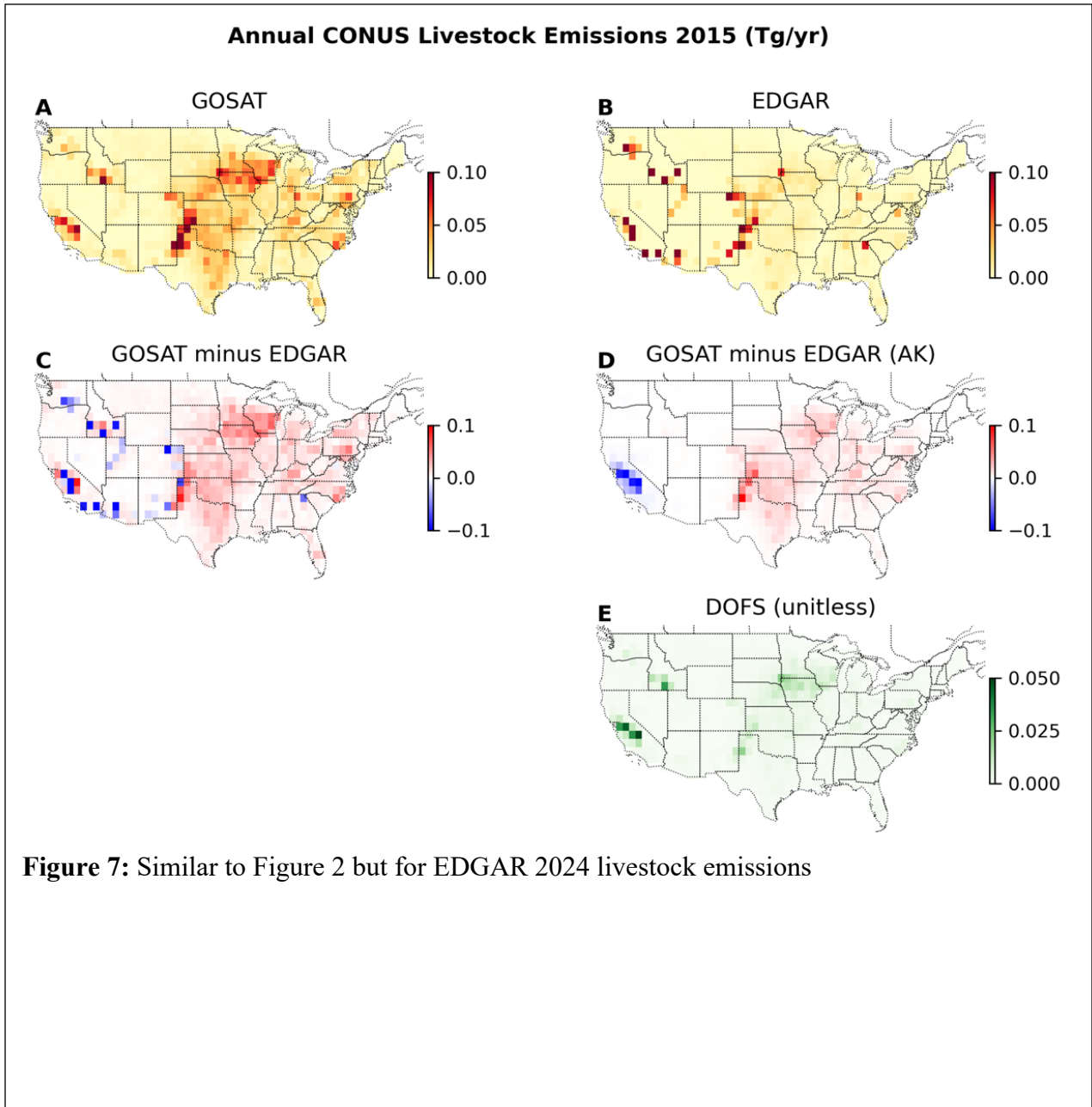


Figure 7: Similar to Figure 2 but for EDGAR 2024 livestock emissions

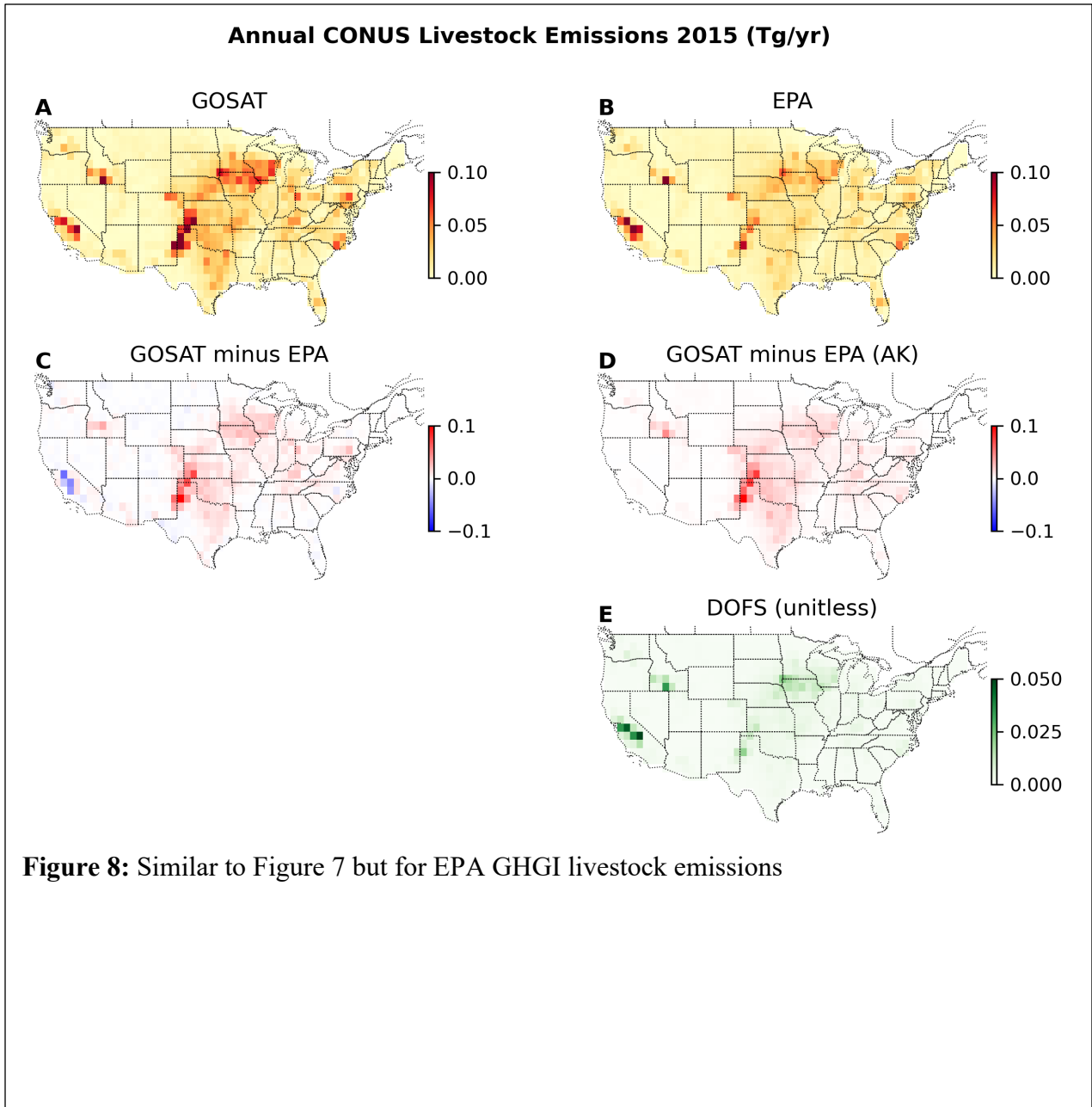
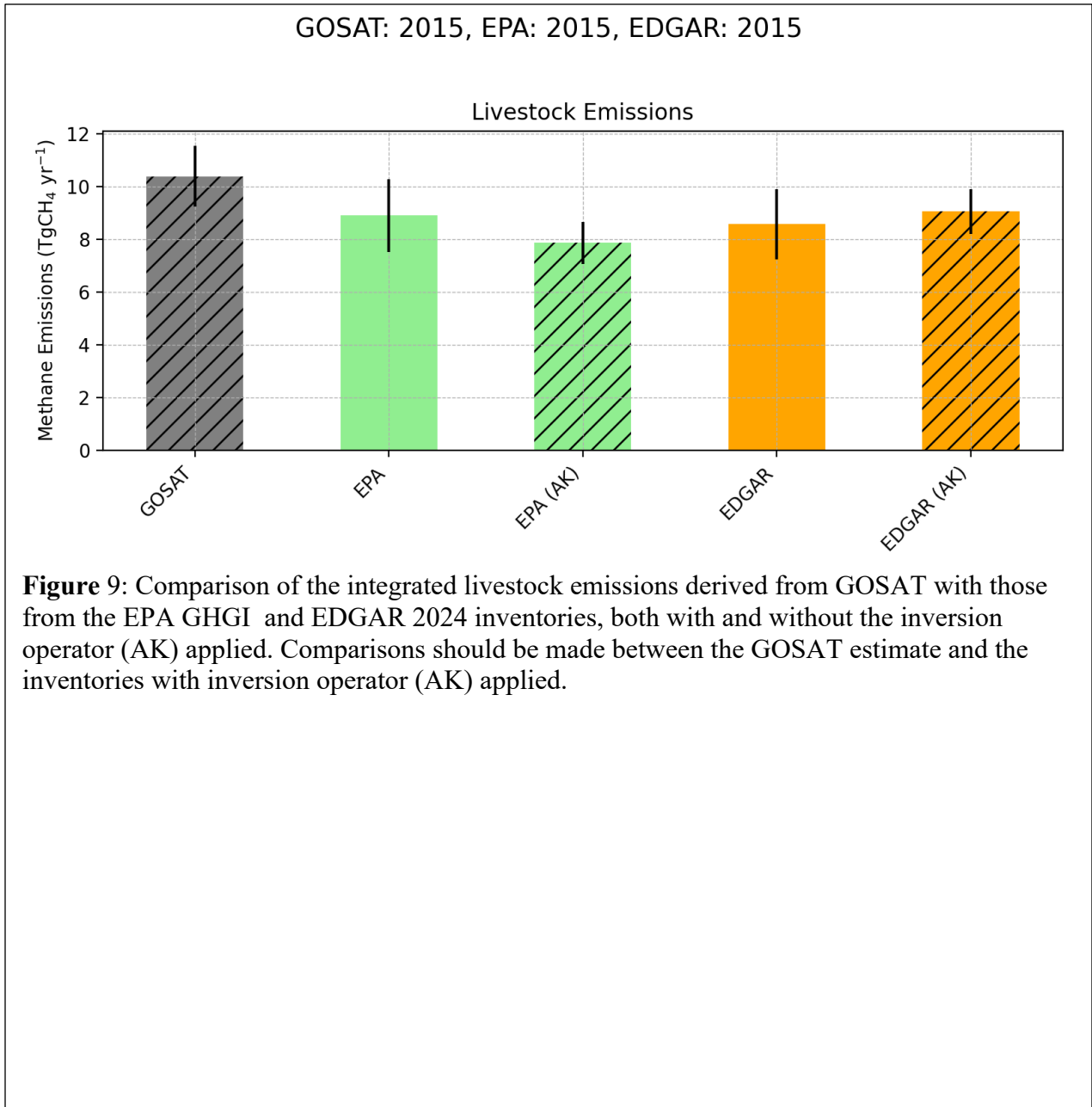


Figure 8: Similar to Figure 7 but for EPA GHGI livestock emissions



997
998
999
1000
1001
1002

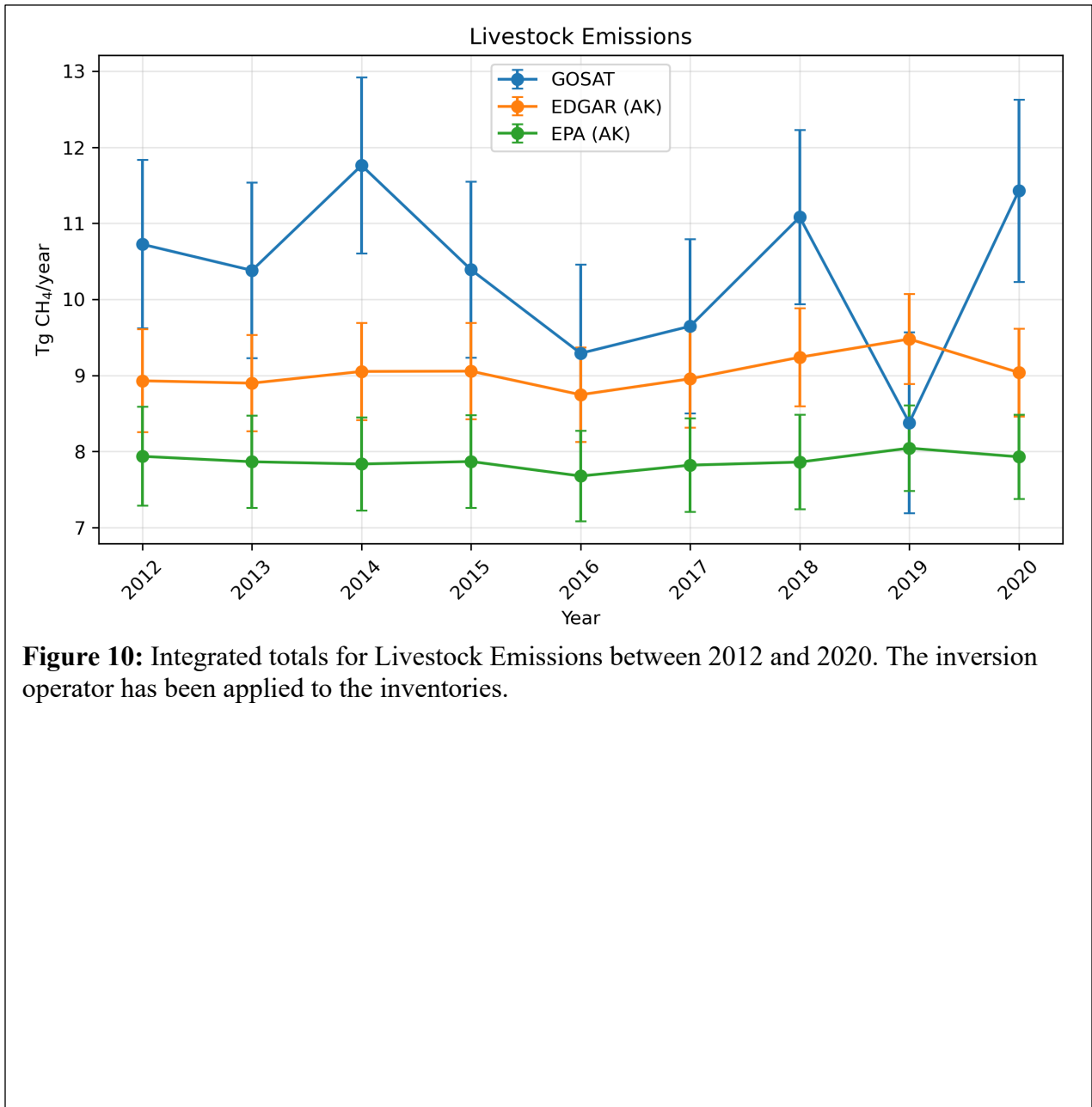


Figure 10: Integrated totals for Livestock Emissions between 2012 and 2020. The inversion operator has been applied to the inventories.

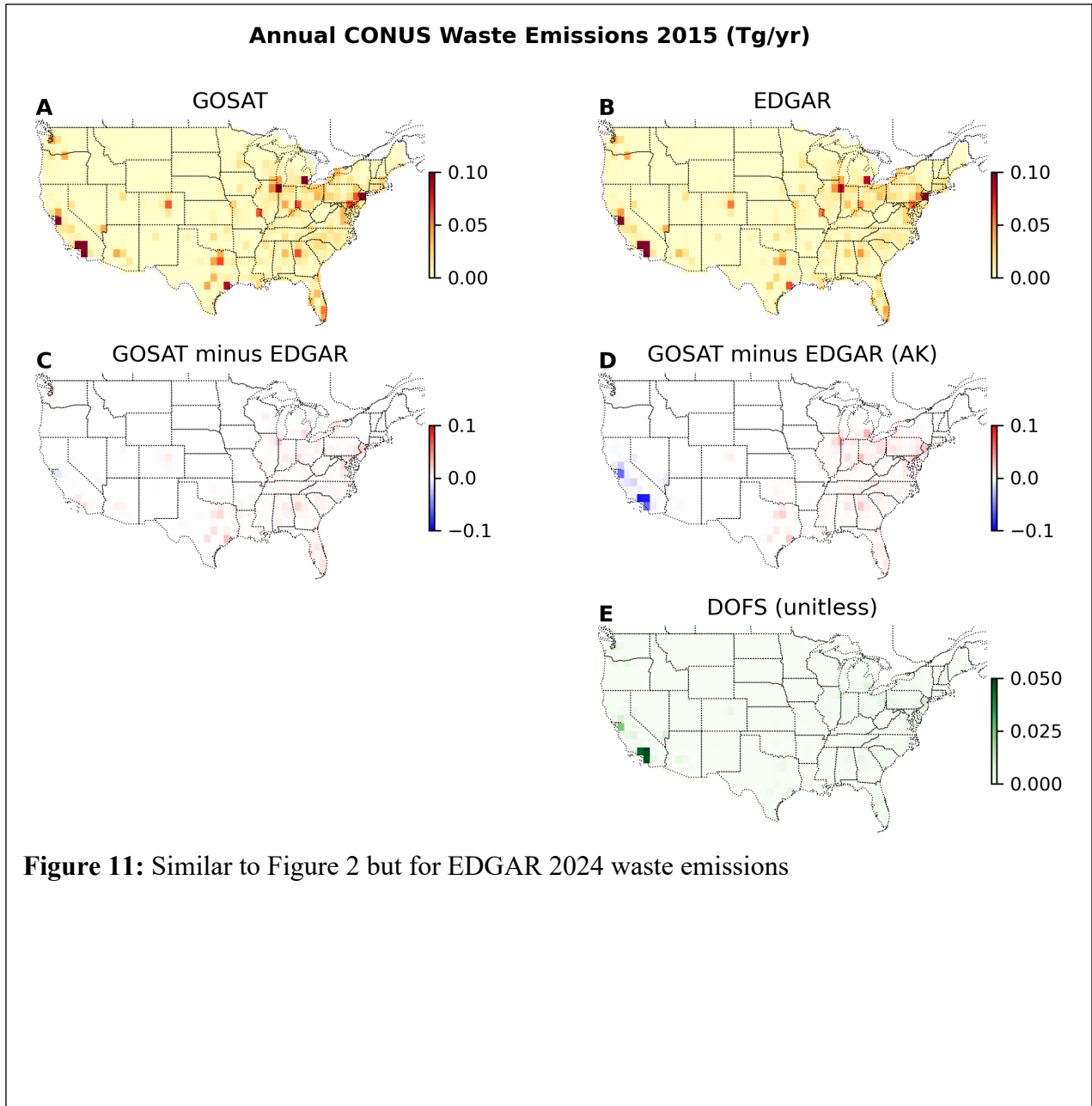
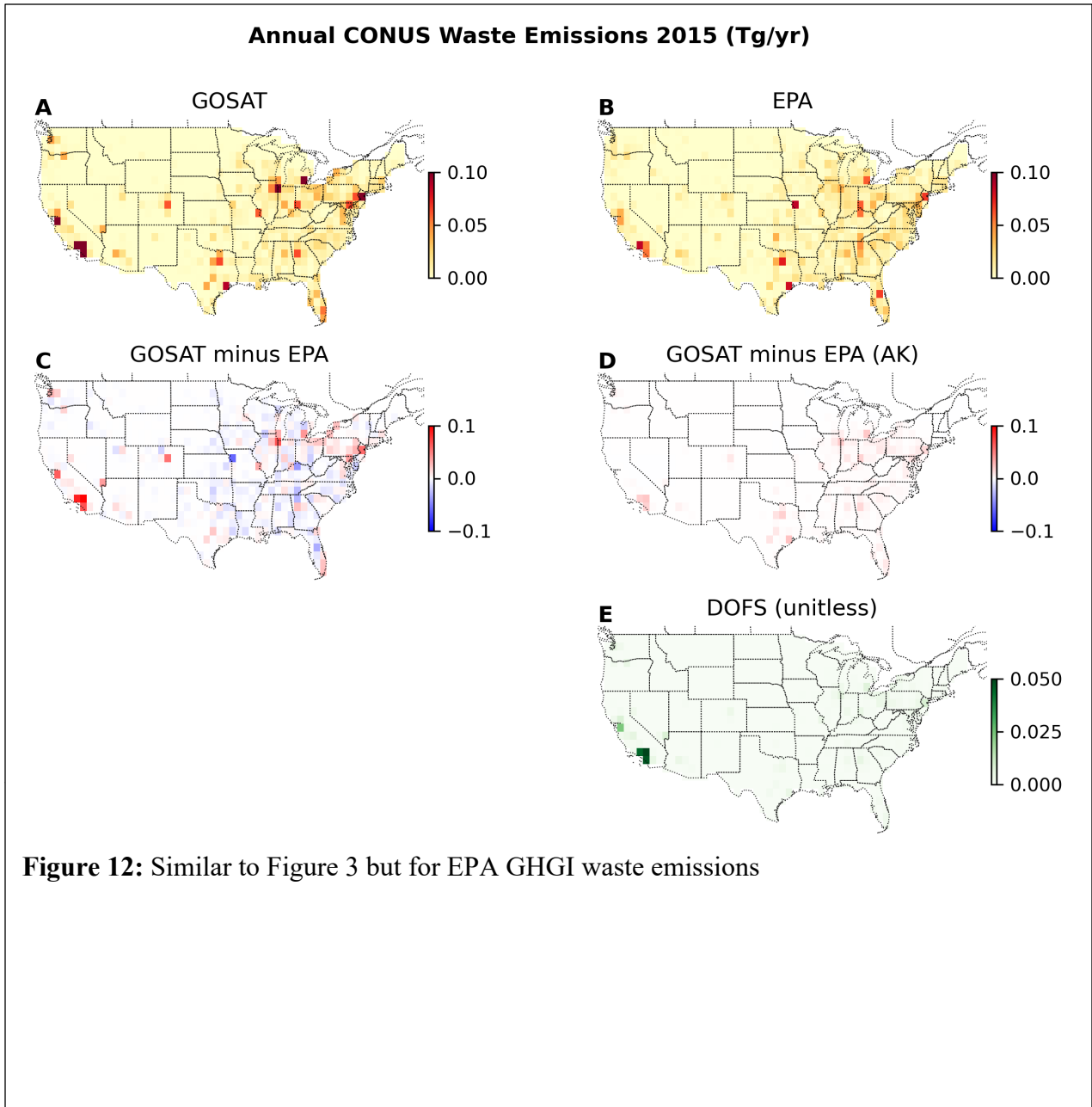


Figure 11: Similar to Figure 2 but for EDGAR 2024 waste emissions

1004
1005
1006
1007



1008
1009
1010
1011
1012
1013

Figure 12: Similar to Figure 3 but for EPA GHGI waste emissions

1014
1015
1016
1017

